ENERGY HARVESTING THROUGH WIND EXCITATION OF A PIEZOELECTRIC FLAG-LIKE HARVESTER

by

ANDREW TRUITT

NIMA MAHMOODI, COMMITTEE CHAIR
KEITH WILLIAMS
STEVE SHEPARD
PAUL HUBNER

A THESIS

Submitted in partial fulfillment of the requirements
for the degree of Master of Science in the
Department of Mechanical Engineering
in the Graduate School of
The University of Alabama

TUSCALOOSA, ALABAMA

2013

ABSTRACT

This study seeks to propose a novel approach to wind-based piezoelectric energy harvesting. A brief literature review of energy harvesting followed by a discussion of piezoelectric system dynamics is offered. Biomedical applications for piezoelectric energy harvesting are then presented offering a segue into fluid based energy harvesting. Fluid based energy harvesting is a relatively young subfield within piezoelectric energy harvesting, but it is increasingly pursued due to the ubiquitous nature of the excitation source as well as the strong correlation with other types of excitation. Vortex-induced vibrations (VIV), as well as vibrations induced by bluff bodies, and the effect of their shape on potential gains have been investigated. The interactions of VIVs on a flag-like membrane form the foundation for the piezoelectric energy harvester in this study. Polyvinylidene fluoride (PVDF) piezoelectric energy harvesters are chosen due to their desirable flexibility. Modeling of flag-like systems is review followed by system modeling of a PVDF piezoelectric flag. Numerical and experimental results from the PVDF flag-like piezoelectric energy harvester are generated and compared. A maximum power output of 1.5 mW is achieved with the flag-like system which is competitive when compared to power output and energy density levels of other studies. The power output of this system provides concrete evidence for the effective use of not only this type of energy harvester system model but also for the use of PVDFs in wind-based applications.

DEDICATION

This thesis is dedicated to my incredible fiancée and family without whom I could not succeed. Your words of encouragement and belief in me constantly provided a source of inspiration and drive. It has been quite a long journey and I feel that we have braved it together. I look forward to the journey ahead and know that with you all in my corner I can accomplish anything.

LIST OF ABBREVIATIONS AND SYMBOLS

$\Psi(x)$ Mode shapes

$\Phi(x)$ Special function for u prior to the comparision function

∇ Del operator

Δp Pressure term due to fluid flow

β Beta value

ε^T Dielectric constant (permittivity) under constant stress

ρ_f Density for flag

ρ_p Density for piezoelectric

ρ Fluid density for Naiver-Stokes

ρ_{air} Density of air for effective mass

A is the maximum amplitude for effective mass

b Width [m]

c_{11} Stiffness of piezoelectric

c^E Young's modulus under an electric field of zero

c Elastic stiffness under a constant electric field

C Capacitance of the transducer

d Width for effective mass

d_{31} Piezoelectric constant (m/V or Coulomb/N)

Dh Hydraulic diameter

e_{33} Product of the piezoelectric constant and young's modulus

e Piezoelectric stress constant,

E_f Young's modulus for flag

E_p Young's modulus for piezoelectric

E_3 Electric field in the three direction

fs vortex shedding frequency

$f\dot{\Delta}$ Mechanical power

f Body forces for Navier-Stokes

h_p Thickness of piezoelectric element [m]

h_f Thickness of flag

H Width for slender wing theory

I_f	Moment of inertia for flag
I_p	Moment of inertia for piezoelectric
k	Eletromechanical coupling factor
K_a	Stiffness with a short-circuited electrode
L	Length
m_a	Effective mass represented by the equation below for slender flags
m_{flag}	Mass of the flag
M	Added mass for slender wing theory
n	Number of piezoelectric material stacks.
p	Pressure for Navier-Stokes
$PVDF$	Piezoelectric terms through analysis
Q	Total electric charge of the electrodes of the transducer
R	Variable used to condense the relationship between C_3 and C_4
s^E	Compliance when the electric field is constant (inverse of the Young's modulus)
S	Strain
S_1	Strain along the axis of the bar.

T	Tension in flag
T	Kinetic energy in Hamilton
U_∞	Free stream velocity for effective mass
U	Potential energy in Hamilton
Vi	Electric power
v	Flow velocity for Navier-Stokes
W_e	Work due to non-conservative forces
dW	Net work
w	Deflection in the z-direction for effective mass
x	Distance along the initial plane of the flag for effective mass
z	Height

ACKNOWLEDGMENTS

I am pleased to have this opportunity to thank the many colleagues, friends, and faculty members who have helped me with this research project. I am most indebted to Dr. Nima Mahmoodi, the chairman of this thesis, for sharing his research expertise and wisdom. You held me to very high standards from the beginning and have taught me the skills to hold myself to those same standards. I could not have asked for a better graduate advisor. I would also like to thank all of my committee members, Dr. Steve Shepard, Dr. Keith Williams, and Dr. Paul Hubner for their invaluable input, inspiring questions, and support of both the thesis and my academic progress.

This research would not have been possible without the support of my friends, fellow graduate students, my family, and of course my fiancée Lauren Tomlinson who never stopped encouraging me to persist. She deserves special credit for patiently waiting for the rare breaks in our busy schedules to spend time together. My Mother and Father have always been supportive of my endeavors and their counsel has never failed to be useful. Logan Wynn, Gary Frey, and Isaac Heim offered their support in the gathering and analysis of data for many days and nights. Their hard work and friendship helped to lighten the load tremendously.

Finally, I would like to thank The University of Alabama Graduate School and the Department of Mechanical Engineering for tuition assistance, the opportunity to be a graduate teaching assistant, and the opportunity to pursue my graduate degree.

CONTENTS

LIST OF TABLES

LIST OF FIGURES

CHAPTER 1

INTRODUCTION

1.1 Problem Statement

This study analyses the use of a PVDF piezoelectric material paired with a flag-like membrane to form a wind-based energy harvester. The impetus for the design was the flapping of a flag in the wind. While many energy harvesting systems, including fluid based systems, use some form of a cantilever beam as a basis, this study uses a flag-like membrane as the foundation. The choice of a flag as the basis for a system model offers a couple unique challenges. In addition to the existing mechanical and electrical dynamic systems of a piezoelectric energy harvester, there is a third dynamic effect from the fluid flow itself. This creates a three-way coupling effect that changes the system equation of motion and forcing function. Additionally, the choice of a membrane, rather than a beam, can also change the equation of motion given certain assumptions. While many studies have been conducted over the years regarding the dynamics of a flapping flag it remains a debated topic. Furthermore, the study of piezoelectric energy harvesters using membranes has until now been limited to hydrodynamic applications.

For a flag-like harvester to work it was hypothesized that an extremely flexible piezoelectric material would be required. Currently the only piezoelectric material with extreme flexibility is PVDF. However, PVDFs are often overlooked as energy harvesters due to their relatively low piezoelectric coefficients when compared to PZTs. Since PZTs are far too rigid, MFCs were chosen as the next best competitor for the given system.

The study includes the derivation of the equation of motion for a flag-like piezoelectric energy harvester as well as overall system response. This is correlated to experimental data but

limited to system frequency response. Mode shapes are not experimentally tested due to a lack of a viable measurement process at the time. The voltage response of the flag-like system is gathered at varying velocities with and without various bluff bodies. The use of bluff bodies is not fully explored in this work but rather introduced experimentally to gauge initial system impact.

The overall goal is to develop a working system model, test the model experimentally, and determine if the power production of the flag-like system is comparable to the output of other fluid based systems. If desirable power levels are achieve, following works will focus on the optimization of the system model, additional measurements of the experimental system, as well as further investigation into the influence of bluff bodies on system response.

1.2 Literature Review

The exploration of renewable, sustainable, and green energy resources is currently one of the most critical challenges that we as a society face. In addition to the well known macro-scale resources such as petroleum, coal, hydro-electric, natural gas and nuclear [1]; active research and development is ongoing in the exploration of alternative energy resources such as solar, geothermal, biomass, nuclear (small scale), wind, and hydrogen [2]. On the microscale and nanoscale newer technologies such as piezoelectric energy harvesters are being researched for advanced and upcoming wireless sensor networks, micro-electromechanical devices, and biosensors [3]. Currently, wireless sensor networks [4] are limited by batteries due to inherent economical constraints of replacing hundreds or thousands of batteries. Onsite energy generation would not only save money through the elimination of batteries but also through the elimination of thousands of feet of wiring currently needed for such networks.

As unmanned aerial vehicles (UAV) decrease in size they will require on board energy regeneration to supplement conventional batteries to increase operational time [5]. These quickly developing UAVs are approaching the microscale and someday even the nanoscale scale. A nano-robot, for example, is proposed to be a smart machine that may be able to sense and adapt to the environment, manipulate objects, take actions, and perform complex functions, but a key challenge is to find a power source that can drive the nano-robot without adding much weight [6]. DARPA is testing its next generation of biomimetic microscale UAVs by using insects and their motions as a system model [7]. Green June beetles have been outfitted with piezoelectric generators that harvest energy from wing movement. This has been shown to produce as much as 115 microwatts in optimum conditions and could be sufficient to power future UAVs of similar size [8]. Other examples include implantable medical biosensors that are rapidly becoming commonplace [9]. For nano-systems it is highly desirable, and often a necessity, to have on board power generation. This is due to weight, packaging, and servicing requirements. Energy harvesting devices are perhaps best suited to the microscale and nanoscale due to the simple fact that they most often operate most efficiently in the μW to mW range. Power output in this range has been proven to be achievable from piezoelectric energy harvesting systems [10].

Vibrations are common throughout industrial equipment, cars, planes, boats, and even civil structures [11-13]. Since kinetic energy is derived from motion it follows that the energy generated by kinetic energy harvesting depends on amplitude and type of vibration present. Additionally the efficiency of the generator itself comes into play when discussing coupling; that is to say that the design of the harvester should maximize the coupling effect between the energy source and the transduction mechanism [14]. Thermoelectric, electromagnetic, and piezoelectric are all examples of transduction mechanisms. The yield from the piezoelectric system as well as

system configuration (coupling) will vary depending on transduction medium. Piezoelectric transduction uses displacement as the coupling configuration parameter and has been shown to achieve desirable outputs in a variety of applications [10, 15, 16].

The piezoelectric effect, or the separation of charge within a material as a result of an applied strain, was first discovered by Jacques and Pierre Curie in 1880 [17]. They discovered that if certain crystals such as quartz were subjected to mechanical strain, they became electrically polarized and the degree of polarization was proportional to the applied strain. Conversely, these materials deform when exposed to an electric field. However, the converse effect was not discovered by the Curie brothers, but mathematically deduced by Gabriel Lippman from thermodynamic principles. Later, the Curie's went back and proved the converse effect in application [18]. These effects are illustrated in Figure 1. Piezoelectric materials come in many forms including high-output single crystals such as PMN-PZT [19], piezoceramics such as lead zirconate titanate or PZT [15], bimorph Quick Pack (QP) [20], Microscale Fiber Composites (MFC) [21], and film based PVDFs. Piezoelectric materials typically exhibit anisotropic characteristics; thus, the properties of the material differ depending upon the direction of forces and orientation of the polarization and electrodes. The anisotropic piezoelectric properties of the ceramic are defined by a system of symbols and notation and are discussed further in the next section. This is related to the orientation of the ceramic and the direction of measurements and applied stresses/forces. The power output achieved in the compressive mode can be improved by increasing the piezoelectric element's thickness or by using multi-layer stacks. Compressive loading, however, is not a practical coupling mechanism for vibration energy harvesting in the majority of applications. Typically, in the case of piezoelectric films or piezoelectric elements bonded onto substrates, the elements are coupled in

the transverse direction. Such an arrangement provides mechanical amplification of the applied stresses.

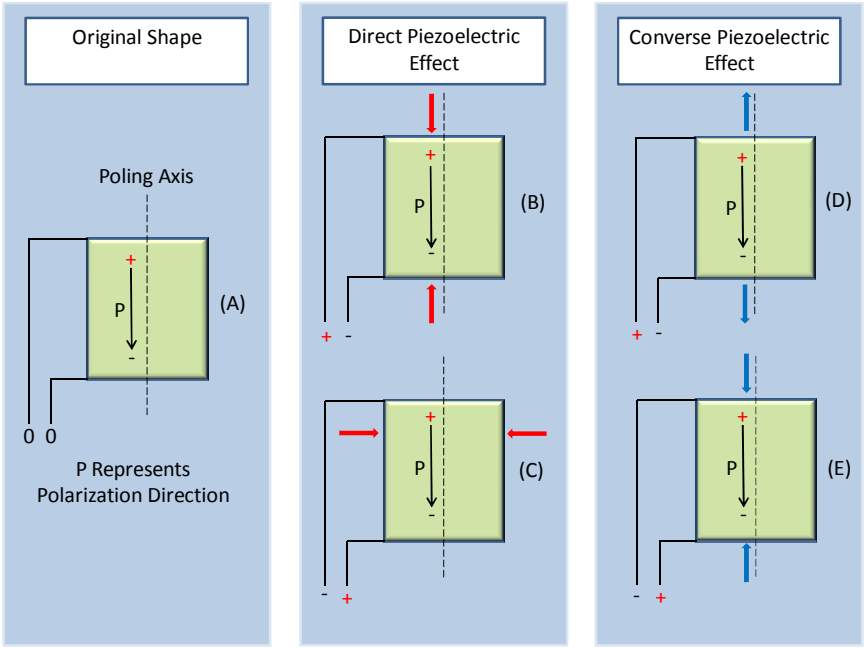

Figure 1. Illustrated piezoelectric effect [22].

Another important constant affecting the generation of electrical power is the electro-mechanical coupling coefficient. This describes the efficiency with which the energy is converted by the material between electrical and mechanical forms in a given direction. Studies investigating the efficiency of a piezoelectric stack operated in compression found that the efficiency was maximized at frequencies several orders of magnitude below the resonant frequency [23]. The load being placed in parallel with the capacitance of the piezoelectric stack was the main contributor towards this effect. Efficiency was also found to increase with increasing force and load resistance but these factors are less significant than frequency. The piezoelectric properties vary with age, stress and temperature [14]. The change in the properties of the piezoelectric material with time is known as the aging rate and varies with construction methods and the material type. The changes in the material tend to scale logarithmically with time so

manufacturers usually specify the piezoelectric constants of the material after material stabilization. The aging process is accelerated by the amount of stress applied to the material and this should be considered in cyclically loaded energy harvesting applications.

A variety of harvesters have been created and tested over the past couple of decades. The earlier types typically used direct actuation from environmental-based vibrations or impacts. This was modeled and simulated by dropping a 5.5 gram steel ball bearing onto 20mm piezoelectric transducer [24]. The optimal efficiency from the impact was found to be 9.4% while using a resistive load of 10 kΩ. The lower efficiency value is due to most of the energy being returned to the ball bearing after the initial impact. In the event of an inelastic collision the efficiency could theoretically approach 50%. Later research explored the possibility of pairing the impact driven piezoelectric harvester with an energy storing device [25]. The storage device chosen was a 1 μF capacitor. The capacitor was also attached to a battery as a further means of storage. The use of energy storage devices in conjunction with piezoelectric harvesters has been thoroughly investigated, and it has been determined that many types of harvesters can successfully charge batteries as well as capacitors [26].

Currently the vast majority of piezoelectric energy harvesting devices use a cantilever beam structure. Since the first resonance of a cantilever beam carries the largest amount of energy, harvesters are generally designed to operate in the first resonant mode [27]. A typical piezoelectric vibration-based generator uses a double-layered piezoelectric beam with a mass at the end. When the beam bends downward, the upper piezoelectric layer is under tensile strain and the lower layer is under compressive strain, resulting in a positive and negative voltage, respectively, across the beam. The mass oscillates back and forth; an alternating voltage is output. This approach has been the basic principle for converting mechanical vibration energy

into electricity for micro-systems. This design has been one of the major micro-generators for mobile and wireless electronics. At the nanoscale gravity no longer plays a significant role in actuation and, therefore, the system depends solely on outside disturbances [6].

Typically, a proof mass is added to the free end of the beam to increase deflection. This lowers the resonant frequency of the beam and increases the deflection of the beam as it vibrates. The larger deflection leads to more strain and, consequently, a higher output voltage and power [27]. Electrodes covering a portion of the cantilever beam are used to conduct the electric charges produced to an electrical circuit, where they can be utilized to charge a capacitor or drive a load. Different electrode lengths or shapes have been shown to affect the output voltage since strain is not uniform across the beam [28]. The electrode shapes as well as their impedance causes additional damping that must be taken into design considerations.

The goal of any energy harvester is to maximize the energy harvested for a particular system. This most often requires matching the natural frequency of the mechanical oscillator to the external forcing frequency as well as the accompanying charge circuit parameters [29-32]. Such a tuned system is able to efficiently transfer energy from the environment to the attachment for electromechanical conversion. This transfer is most efficient, with the accompanying largest vibrational amplitude, when the inherent mechanical damping is low [33]. However, such lightly damped systems are also characterized by their sharp resonant peak. If there is any mistuning relative to the target frequency, then the efficiency of the system will suffer. To overcome this sensitivity to frequency mistunings, nonlinear mechanical attachments have been proposed as the basis for energy harvesting systems [34-36]. These nonlinear systems are often more versatile than their linear counterparts since they operate over a wider range of forcing frequencies.

CHAPTER 2

DYNAMICS OF PIEZOELECTRIC ENERGY HARVESTERS

When modeling the entire dynamic system of a piezoelectric energy harvester one must also consider the dynamics of the piezoelectric actuator. As previously discussed, the piezoelectric effect is an electromechanical phenomenon that occurs when a coupling of electrical and mechanical states occurs due to an applied mechanical stress to dielectric crystals. Conversely, if electrical differential is supplied to the piezoelectric then the system will respond with a mechanical stress in the form of a material deflection. This direct and converse effect makes piezoelectric materials valid for both sensors and actuators. To further understand the operating effects shown in Figure1, the following coupling equations can be used with the first equation representing the direct effect (i.e., sensing mechanism) while the second equation denotes the converse effect (i.e., actuation mechanism) [37]

$$D = \varepsilon^T E + d_{ij} T \tag{1}$$

$$S = d_{ij} E + s^E T \tag{2}$$

where D is the electric displacement (Coulombs/m^2), ε^T is the dielectric constant (permittivity) under constant stress, E is the electric field (V/m), T is stress (N/m^2), d_{ij} is the piezoelectric constant in the ij direction (m/V or Coulomb/N), S is the strain, and s^E is the compliance when the electric field is constant (inverse of the Young's modulus).

The different piezoelectric materials can be compared using an electromechanical coupling factor. This factor measures the efficiency of the material to convert mechanical energy into electric energy. The equation to calculate the electromechanical coupling factor is given below

$$k^2 = \frac{d_{33}^{\ 2}}{s^E \varepsilon^T} = \frac{e_{33}^{\ 2}}{c^E \varepsilon^T} \tag{3}$$

where k is the eletromechanical coupling factor, c^E is the young's modulus under an electric field of zero, and e_{33} is the product of the piezoelectric constant and young's modulus. The typical values of *k* range from 0.3 to 0.7. The *k* value will also affect the way the stiffness is affected by boundary conditions [38]. When *k* is large, there will be a great change in stiffness with respect to the electrical boundary conditions. The capacitance also follows a similar approach. The capacitance will depend on the mechanical boundary conditions. It is possible to further increase this *k* value by shunting a (synthetic) negative capacitance to the transducer.

As discussed with Figure 1 and Equations (1-2), there are different operating effects that are dependent on input. Additionally, there are different operating modes that depend on input. Figure 2 illustrates the 33 and 31 operating modes. In the 33-mode the applied force and subsequent voltage generated act in the same direction. This type of loading typically uses piezoelectric stack-style actuators. Conversely, if piezoelectric bimorph actuators are used, then the 31-mode is utilized. The applied force and generated voltage act perpendicular to one another.

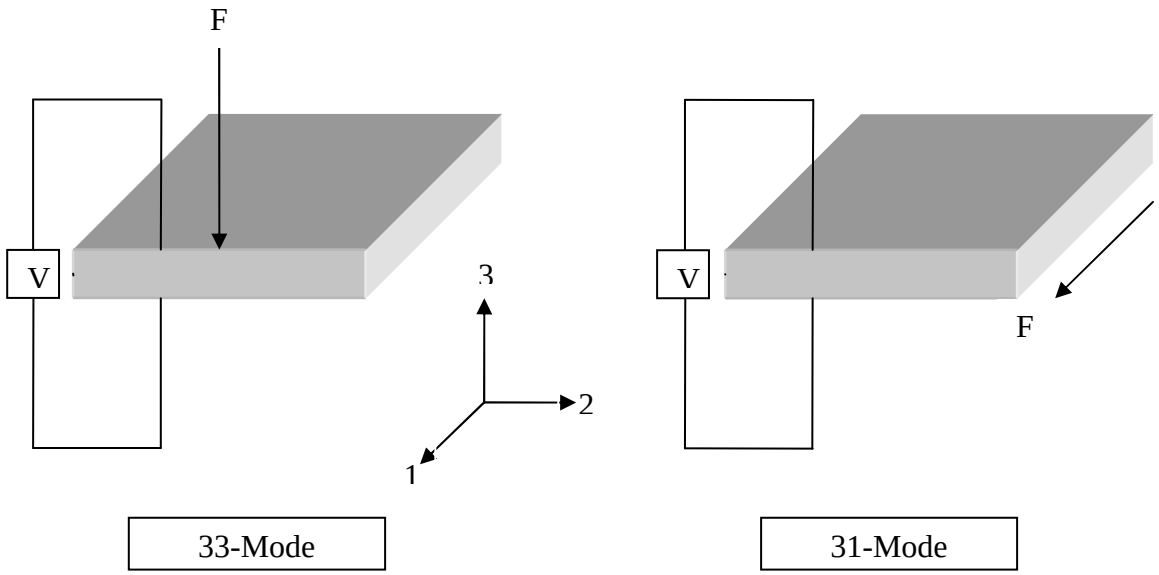

Figure 2. Operating modes of a piezoelectric transducer.

Operating mode, piezoelectric material type, mounting location, and system parameters are all considered when determining the performance of a piezoelectric system. Additionally the sensor itself is subject to nonlinearities due to stress-strain relationship as well as the electromagnetic coupling between the generator and the beam [39]. From a modeling point of view, the actuation force comes through the piezoelectric layer; hence, the stress–strain relations are related to actuation voltage and electrical properties of the piezoelectric layer [40]. A single degree of freedom cantilever style design is one of the most straight forward examples and allows a basic understanding of the governing principles that can be used to understand more complex dynamic systems. Figure 3 represents a single degree-of-freedom system with the unidirectional response of the system acting in the Y direction. The cantilever beam with a proof mass shown in Figure 3a is equivalent to the single degree of freedom system shown in Figure 3b.

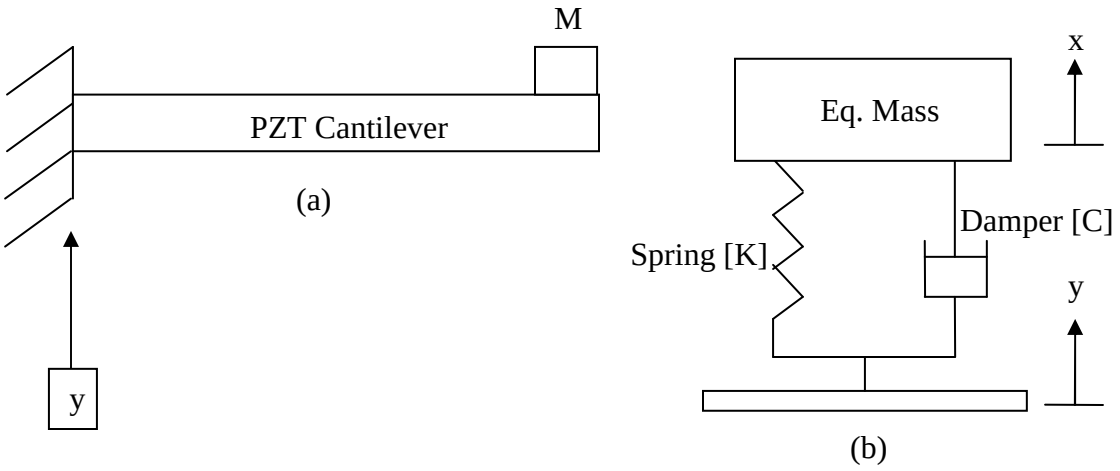

Figure 3. Cantilever beam with tip mass (a) and equivalent lumped spring, mass, and damper system with base excitation (b).

The characteristic behavior of a given system can be simplified to two base parameters: damping constant and natural frequency [37]. The mass or lumped mass, spring stiffness, and damping coefficient are represented in variable form by *M*, *K*, and *C* respectively. Energy balanced computational techniques or d'Alembert's principle can be used to derive the equation of motion. The following equation of motion is valid for systems (a) and (b) and follows:

$$M\ddot{z} + C\dot{z} + Kz = -M\ddot{y} \tag{4}$$

where $z = x - y$ is the net displacement of the mass. This can also be rewritten using the two base parameters of damping constant and natural frequency

$$\ddot{z} + 2\zeta\omega_n \dot{z} + \omega_n^2 x = -\ddot{y} \tag{5}$$

where ζ is the damping ratio and ω_n is the natural frequency of the system. The maximum power that can be achieved by the system is [14]:

$$P_{\max} = \frac{MY^2 \omega_n^3}{4\xi} \tag{6}$$

Maximum power is realized when the natural frequency is the operating frequency as discussed in the previous paragraph. Resonant frequencies of a beam can be determined using the Euler-Bernoulli beam equation. When appropriate end conditions are applied, the calculated eigenvalues can be used to find the resonant frequencies of the system [41]

$$\frac{\partial^4 \varsigma}{\partial^4 x} + \frac{\rho A}{EI} \frac{\partial^2 \alpha}{\partial t^2} = 0 \tag{7}$$

where α is the beam deflection (a function of position along the beam and time), ρ is the density, *A* is the area of the cross section of the beam, *E* is the Young's modulus, and *I* is the area moment of inertia. The specific derivations of equations of motion for a cantilever design system with proof mass can be found in [37]. In addition to different loading scenarios research has also been done investigating multiple proof mass systems [42].

Linear conditions are ideal and allow for easier computation but do not represent the true model of most energy harvesting systems. If a given system only operates at a single frequency, then the energy harvesting system can be optimized to work with that frequency. Nonlinear vibrations usually generate high amplitude deformations which provide a better efficiency for energy harvesters. Research into the nonlinearities of piezoelectric dynamic systems has been conducted in reference to atomic force microscope applications [43], micro-cantilevers [40, 44] , and active vibration control [45]. Magnetic nonlinearities have also been studied as a way to increase the operating bandwidth of piezoelectric energy harvesters [36, 46-48]. Recent work offers significant advances over previous works through the inclusion of nonlinear electric

coupling when modeling system behavior [47]. Conditions for which bifurcation and instability may occur are discussed in this study along with supporting data. All investigations indicate performance gains to varying degrees and a particular benefit to systems with slow varying frequencies. Recently, nonlinear models for aeroelastic energy harvesters have been investigated, which shows that quadratic nonlinearity appears due to plunge and pitch motions [49, 50] . In addition, when a tip mass is used in a harvester, a cubic nonlinearity appears in the equations of motion due to inertia [51].

These outcomes, although representative of macro-scale harvesters, can also be applied to microscale harvesters. MEMS deformation can also be nonlinear which affects the microscale energy harvesters. In a series of theoretical studies, the equations of motion for the nonlinear flexural-flexural-torsional free vibrations of inextensible piezoelectrically-actuated Euler-Bernoulli microbeams were derived and investigated [40, 52]. The model included both geometric and inertia nonlinearities due to large deformation of a piezoelectric microcantilever beam but did not include the material nonlinearities by assuming linear constitutive equations shown in Equations (8) and (9) [53]. The piezoelectric material can also produce nonlinear terms if the nonlinear constitutive equations are used [44]

$$\sigma_{11}^{p} = E_{p}\varepsilon_{11}^{p} - h_{31}Q_{3} + \frac{\alpha_{1}(\varepsilon_{11}^{p})^{2}}{2} + \frac{\alpha_{2}Q_{3}^{2}}{2} - \alpha_{3}Q_{3}\varepsilon_{11}^{p} \tag{8}$$

$$D_{3} = h_{31}\varepsilon_{11}^{p} + \beta_{31}Q_{3} + \frac{\alpha_{3}(\varepsilon_{11}^{p})^{2}}{2} + \frac{\alpha_{4}Q_{3}^{2}}{2} - \alpha_{2}Q_{3}\varepsilon_{11}^{p} \tag{9}$$

where suffix p is for piezoelectric, E is the modulus of elasticity, ν is its Poisson's ratio, Q_3 is the applied electric field, D_3 is the electric displacement, β_{31} is the permittivity coefficient, h_{31} is the

piezoelectric constant relating charge density and strain, and the α_i are nonlinear coefficients. The nonlinear equation of motion for a piezoelectric beam including material, geometry, and inertia nonlinear terms can be expressed as [39, 54, 55]

$$\begin{aligned} & m(s)\ddot{v} + \left(K(s)v''\right)'' + \left(\frac{3\alpha_1}{2} I_{np}(s)v''^2\right)'' + \left[v'\left(K(s)v'v''\right)'\right]' \\ & + \left[v'\int_l^s m(s)\int_0^s \left(\ddot{v}'v' + \dot{v}'^2\right)dsds\right]' - \left[\frac{1}{2}v'\left[K_p(s)v'P(t)\right]'\right]' \\ & + \left[\frac{1}{4}K_p(s)v'^2P(t)\right]'' = \left[\frac{1}{2}K_p(s)P(t)\right]'' \end{aligned} \tag{10}$$

$$v = v' = 0 \quad \text{at } s=0; \quad v'' = v''' = 0 \quad \text{at } s=l\,.$$

where *v(t)* is bending vibration, *s* is variable along the length of the beam, *m(s)* is mass density, *P(t)* is voltage, *K(s)*, $K_p(s)$, and $I_{np}(s)$ are dependent on the physical and geometrical properties of the beam and piezoelectric material.

CHAPTER 3

BIOMEDICAL AND BIOENGINEERING APPLICATIONS

The use of wearable energy harvesting systems for powering mobile devices has been investigated in a variety of scenarios [56]. Human motion is often characterized by large amplitude movements at low frequencies such as with walking. This can create difficulties in the design of a miniature resonant generator to work on humans. Coupling by direct straining of, or impacting on, a piezoelectric element has been applied to human applications [56]. Studies have shown that an average gait walking human of weight 68 kg, produces 67 W of energy at the heel of the shoe [57]. While energy harvesting from walking would interfere with the gait, it is clear that there is a potential energy harvesting opportunity. The theoretical limits of piezoelectric energy harvesting on human applications, based upon assumptions about conversion efficiencies, have suggested that 1.27 W could be obtained from walking [58]. One of the earliest examples of a shoe-mounted generator incorporated a hydraulic system mounted in the heel and sole of a shoe coupled to cylindrical PZT stacks [59]. The hydraulic system amplifies the force on the piezoelectric stack whilst reducing the stroke. Initial calculations were performed in order to design a generator capable of developing 10 W. A scale model was built and tested which suggested that 6.2 W could be generated with the full size generator on a 75 kg subject. The generator design was relatively large in size, and as previously mentioned the gait of motion will most likely be affected. These impact driven systems can be modeled and solved using the same modeling and computational methods for the single-degree-of-freedom systems discusses in the previous chapter. Figure 4 shows an example of a shoe based piezoelectric generator.

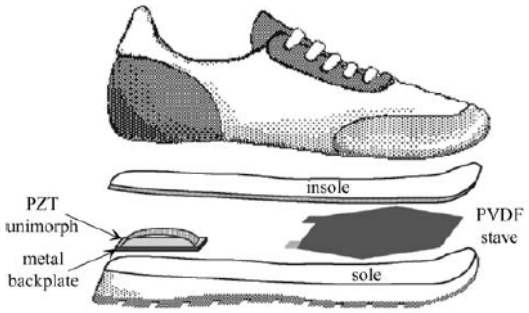

Figure 4. Shoe based piezoelectric generator [60].

In addition to the investigation of energy harvesting using piezoelectric materials through human motion, there has also been an increase in research of health monitoring using piezoelectric materials [9, 57, 58, 61-65]. Many of the same control methods and underlying principles are shared between the controls and harvesting approaches leading to a possible synthesis between the two fields. One such device utilizes piezoelectric sensors to monitor the health of a baby during fetal development [62, 65]. In low risk pregnancies, the continuous monitoring of the fetal health is based on traditional protocols for counting the fetal movements felt by the mother. Although the maternal perception is a relevant characteristic for the evaluation of the fetal health, this kind of monitoring is hard to accomplish and is highly subjective. Therefore, it is important to obtain a universal electronic obstetric tracing, allowing for the identification of sudden changes in the fetus health, by continuously monitoring the fetus movements. The Smart-Clothing project aim has been the development for this purpose. The piezoelectric sensor belt has shown a high capacity to detect fetal movements, isolating them from external interferences. This is achieved through the incorporation of bands of piezoelectric sensors that rely on the direct piezoelectric effect. When the developing fetus moves inside the womb a region of a piezoelectric band will deflect resulting in a subsequent voltage output that can be measured. An example of this system is shown in Figure 5. This data can be downloaded or sent to doctors for

review. While this device does use traditional batteries for power it could no doubt benefit from the incorporation of an energy harvesting system to ensure uninterrupted monitoring. Some of these same technologies (Smart-Clothing) can and are being researched for energy harvesting using body movements such as breathing.

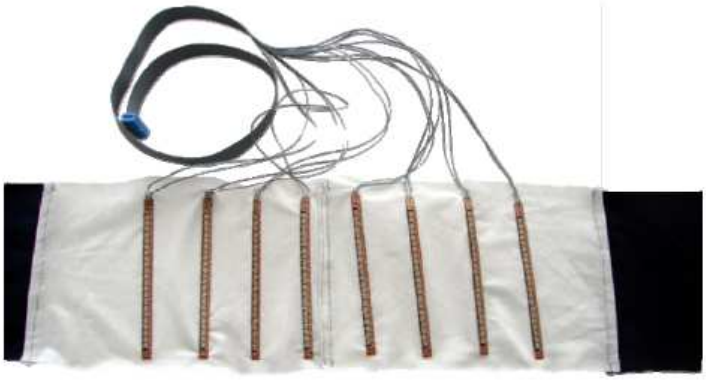

Figure 5. Smart Clothing belt with piezoelectric bands [62, 65].

The generation of power by positioning piezoelectric inserts within orthopedic implants has been studied [66]. These inserts are intended to power sensors that provide *in vivo* monitoring of the implant to reduce future complications. The axial force across a knee joint can reach three times the body weight several times per step. This load was applied across a prototype generator containing three piezoelectric stacks each containing 145 PZT layers. The implant was demonstrated with a 10 μF storage capacitor and a microprocessor periodically switching an LED on during each step. The system was found to deliver 850 μW of continuous regulated power with an electrical efficiency of 19% with the maximum mechanical efficiency being 20% into impedance matched load. Other studies have investigated *in vivo* implants that focus on muscle tissue [67, 68]. These studies focus on the base principle that the electrical energy required to drive a muscles motor nerve is less than the mechanical output power of the given muscle. Based on their modeling and testing, 690 μW of power was generated, which

would be sufficient to power certain generators, or possibly other types of *in vivo* devices. Figure 6 shows a block diagram illustrating the position of the piezoelectric generator within the biological system.

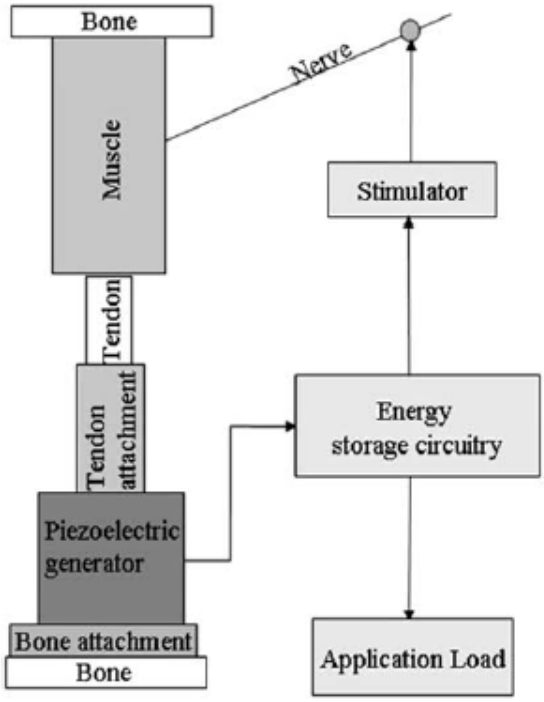

Figure 6. The implantable stimulated-muscle-powered piezoelectric energy generator concept [67] .

Other *in vivo* studies take fluid dynamics of the human body into account [69]. The motivation of this work was the potential for *in vivo* "lab on a chip" or other systems powered from kinetic energy sources. The design used square plate geometry to extract energy from the change of blood pressure with each pulse. A typical blood pressure change of 40 mmHg at a frequency of 1 Hz was used to calculate the power of a range of square plates from 9 μm to 1100 μm thick and with 1 mm to 1 cm side lengths. Maximizing the area and minimizing the plate thickness maximized the calculated power providing a theoretical value of 2.3 μW. Circular and

square PVDF plates for use in harvesting energy from changes in blood pressure have also been investigated [70]. The finite-element analysis of the PVDF membranes determined that for a circular diaphragm of 5.56 mm radius the optimum thickness of 9 μm produces 0.61 μW whilst a 10 × 10 mm square membrane of thickness 110 μm produces 0.03 μW. Experimental tests utilizing 28 μm thick piezoelectric membranes pulsed at 60 Hz by uniform pressure yielded 0.34 μW and 0.25 μW for the circular and square plates, respectively. The use of patterned electrodes and differential poling as shown in Figure 7 could have been employed to increase output.

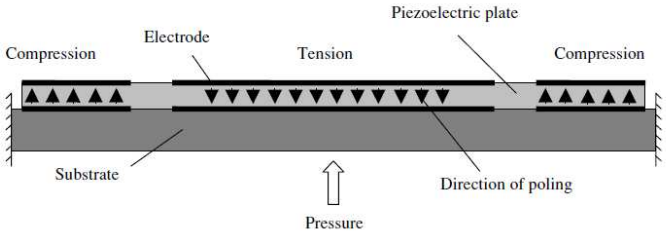

Figure 7. Patterned electrodes and differential poling on membrane [14].

Additional studies have also demonstrated the resourcefulness of piezoelectric energy harvesters in *in vivo* applications through the powering of heart pacemakers by the heart's own vibrations [71]. Pacemakers and Implantable Cardioverter Defibrillators (ICD) have decreased in size and power requirement to such a degree that one microscalewatt is a reasonable upper limit. Using ultrasonic velocity measurements the vibrations of the heart was measured and used to design both linear and nonlinear harvesters. A zigzag structure was used, as opposed to a cantilever design, to allow for a sufficiently low natural frequency of 39 Hz. Because a heartbeat is not steady state a nonlinear design was also investigated. This design incorporated a cantilever beam with a magnetic proof mass and a magnetic frame mass. The opposing forces introduced by the magnets overcomes the restoring force due to beam elasticity, which will then cause the zero deflection position of the system to become unstable. This will allow for two equilibriums

and the system will be efficient over a larger range than the linear system. The linear and nonlinear systems are shown in Figures 8 and 9 respectively.

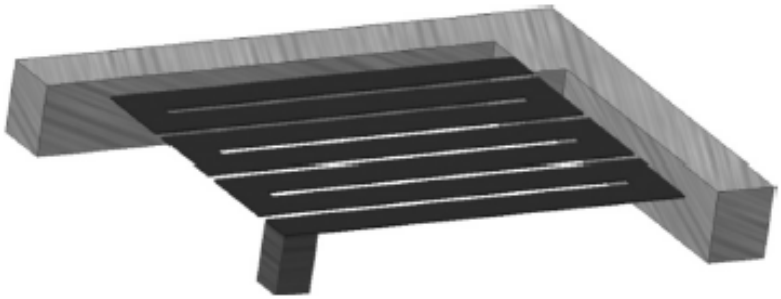

Figure 8. Linear zigzag energy harvester [71].

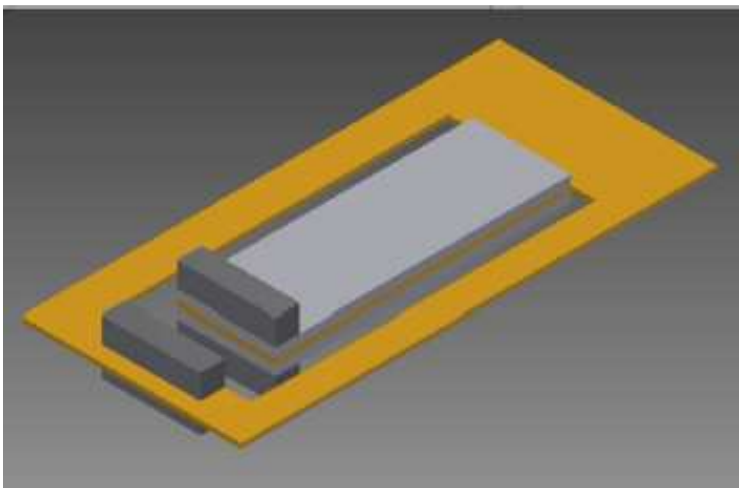

Figure 9. Nonlinear energy harvester with magnets [71].

These examples prove the validity of using fluid flow from the body as a source of energy harvesting. This perhaps could have been assumed given that the human heart is a unique type

of pump but more importantly this also implies that other types of fluid based energy harvesting may be equally rewarding.

CHAPTER 4
FLUID-BASED ENERGY HARVESTING

Fluid based energy harvesting is a relatively new area of excitation research. Fluid as an energy source though is not a novel concept. The two most common types of fluid energy are aerodynamic and hydrodynamic, and some of the earliest representations of these ideas are windmills and dams. The use of hybrid solar-hydroelectric dams is being investigated to further increase the power output and efficiency of dams [72, 73]. Wind turbines have grown in size and output with common turbines in the U.S. producing 1.5 megawatts a piece and next generation turbines expected to produce 10 megawatts a piece [74]. As with dams, there have been, and continue to be, numerous studies into the dynamics and efficiencies of wind turbines [75-78]. Due to their complexity, wind turbines can be downsized but can be subject to detrimental effects on their efficiencies [79]. The current methods of fluid-based energy harvesting are not well suited, or scalable, to meet the demands of the rapidly developing microscale and nanoscale technology markets. To address this, investigation into fluid based piezoelectric energy harvesting began years ago and has slowly developed. Early experiments were inspired by excessive vibrations due to aerodynamic instability phenomena such as vortex-induced vibration, galloping, flutter and buffeting [80].

4.1 Vortex Induced Vibrations

Vortex or flow-induced vibrations (VIV) is perhaps one of the more extensively studied methods of fluid based energy harvesting. The driving principle behind this approach is the creation of periodic amplitudes in a body due to periodic cross-wind forces generated by the shedding of vortices in the wake of the given body [81]. Several studies have been performed on VIVs considering the aerodynamic properties and their effects on the system [82-85]. It is

continually noted that the Reynolds Number and Strouhal number play significant roles in predicting VIV generation. Current methods do allow for fairly accurate predictions of VIVs, but even the most modern methods are still overly simplified through the elimination of several degrees of freedom. This indicates a great potential for further research in the area. In one study a harmonica was used as a source of inspiration for the design and analysis [86]. Operation of the harvester begins when wind enters the chamber and tries to escape through the small opening between the cantilever, in this case a reed-like harvester, and the supporting structure. The rapid change in area causes a flow separation from the cantilever at the sharp edge which in turn causes a rapid increase in velocity. This, in turn, produces a pressure drop across the cantilever. This pressure drop deflects the cantilever which increases the aperture area. Consequently, the flow velocity drops and the pressure drop decreases. The mechanical restoring force, or beam elasticity, pulls the beam back decreasing the aperture area and the process is repeated. These periodic fluctuations in the pressure cause the beam to undergo self-sustained oscillations. The resulting periodic strain in the piezoelectric layer produces an electric field via the direct piezoelectric effect which can then be harvested. Figure 10 depicts the device used in this study.

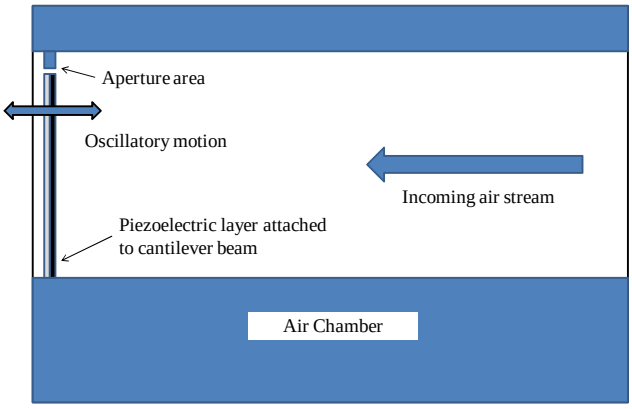

Figure 10. Schematic of harmonica inspired piezoelectric energy harvester [86].

A similar approach with a flow varying pressure chamber has also been studied although the transduction medium in that case was electromagnetic [88]. The proposed Amber Waves of Grain (AWOG) device offers a unique approach of using an array of cantilever piezoelectric beams subject to wind fluid vibrations [89]. While cantilevered designs offer simplified mathematical models, and are often the first models investigated, additional models and computational techniques quickly follow [90-92]. Flexible ceramic cylinders have been subjected to an axial flow that exerts a transverse force on the cylinder due to asymmetrical vortex shedding [92]. This force causes flexural vibrations that are then harvested through piezoelectric generators.

4.2. Bluff Body Effects

The use of bluff bodies to induce vortices is a natural progression of the flow-induced approach and offers advantages in the area of system tuning among others. By placing cantilever beams in the wake of a bluff body vibrations are induced into the structure through vortex shedding. By varying the shape, size, and offset distance of the bluff body the response of the system can be tuned to the natural frequency to obtain maximum energy levels. Furthermore, vortex shedding frequencies in the wake due to the bluff body also depend on parameters such as Reynolds number, Strouhal number, and smoothness of the structure [93]. One study analyzed the effects that different bluff body shapes and system parameters have on energy harvesting [93]. In this study a cantilever beam was attached to the trailing edge of the bluff-body. The system is fully modeled followed by manipulation of the bluff body shape and its particular influence on lock-in region bandwidth. Lock-in is understood to occur when the frequency of the structure matches that of the undisturbed wake behind the bluff body. Lock-in is of particular significance due to the fundamental importance of frequency matching inherent to energy

harvesting as well as the practical problem of fluid flow variations. Realistically, one can expect a fluid flow to be transient, and, therefore, a wideband lock in region is required for any bluff body based energy harvester to be effective. Vortex shedding frequency can be found with the following equation [93]:

$$f_s = \frac{SU}{L} \tag{11}$$

where S is the Strouhal number which can vary with the Reynolds number and bluff body shape, U is flow velocity, and L is the characteristic dimension of the bluff body. While this equation is simple it has profound implications. The conclusion of the study determined that the pentagonal shaped bluff body had the largest lock-in region (Re=300-1800) but the cylindrical bluff body had the highest average power gain (0.35mW). Figure 11 shows vortex generation based on different bluff body shapes. It is also worth noting that the study revealed that once lock-in was achieved, (fs=fn) then the free stream velocity could be altered to a degree without detrimental system performance. This is in direct contrast to the next study discussed.

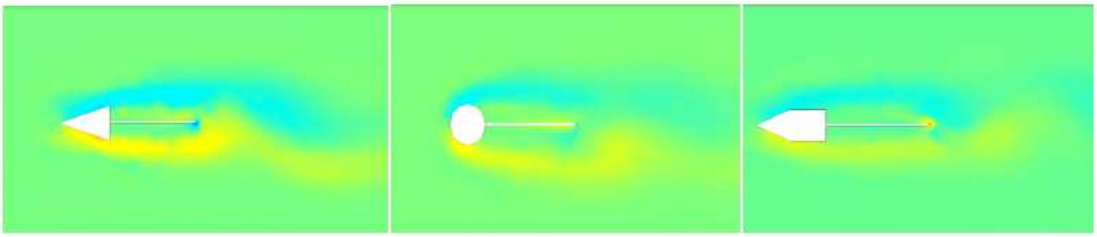

Figure 11. Vorticity field plot [93].

A study of a cylindrical bluff body demonstrated that minor mismatching between the natural frequency of the system and the vortex shedding frequency can have significant detrimental effects on the energy output [94]. This is particularly true when fs<fn for this

particular system. This test was visualized through the use of laser sheet illumination in a wind tunnel. Several configurations of the beam in reference to the flow were explored, but the highest output was achieved with the beam parallel to the upstream flow in a face-on configuration. In a different approach, a cylinder was attached to a hinged splitter plate with piezoelectric elements [95]. The significance of the hinge is that it negates the natural restoring force of the beam found in a system with a rigidly fixed splitter plate.

Thus far, the experiments presented have focused on aero-elastic interactions. One such example that uses hydrodynamic forces is the energy harvesting eel [96]. As with the previously discussed designs this design also incorporates a bluff body. The main difference is that the fluid in this case is water, and the design is developed into a complete system. The purpose was to emulate an eel like life form swimming in a stream or ocean. This is achieved through strips of piezoelectric elements oscillating behind a bluff body complete with on board power storage. A proposed application of this is the powering of oceanographic robots as illustrated in Figure 12.

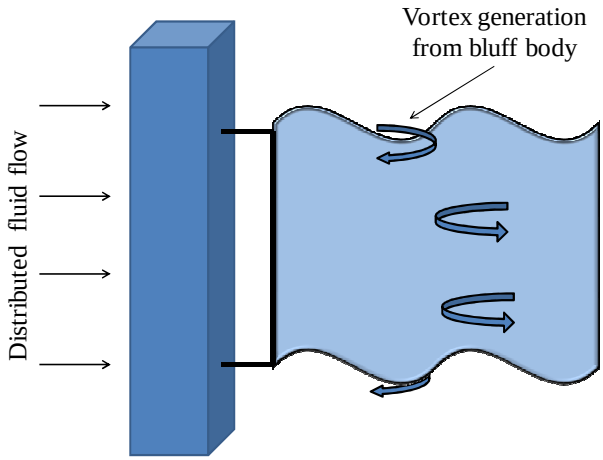

Figure 12. Model of eel energy harvesting system [96].

4.3. Aeroelastic Instabilities and Energy Harvesting

Flutter response is typically categorized as a type of aeroelastic instability. It occurs when there is a positive feedback between the natural frequency of a system and the aerodynamic forces. For flutter, the movement of the object due to oscillation increases with aerodynamic load, which in turn drives the object to move further. If the energy input by the aerodynamic excitation in a cycle is larger than that dissipated by the damping in the system, the amplitude of vibration will increase, resulting in self-exciting oscillation. The amplitude can, thus, grow and is only limited when the energy dissipated by aerodynamic and mechanical damping matches the energy input, which can result in large amplitude vibration and potentially lead to rapid failure [97]. Most flutter-based energy harvesters exploit limit cycle oscillations. Cantilevered plates subject to an axial flow show instabilities at sufficiently high flow velocities. When this happens flutter takes place and energy is continually pumped into the plate from the fluid flow while sustaining flutter motion [98]. This critical flutter speed of the system can further be tuned by the damping caused by piezoelectric coupling [99]. Airfoil-based designs are particularly interesting examples of flutter response based systems due to the combination of several characteristics previously mentioned.

In one study an airfoil was mounted on a beam with a hinged base as shown in Figure 13 [87]. Linear and nonlinear system models were derived for the system to predict the wind speed and flapping frequency corresponding to the onset of flutter. The system eigenvalues were determined as a function of the incident wind speed. Subsequently the flutter boundary is identified as the point where the real part of one of the eigenvalues becomes positive. The flutter frequency can then be found from the imaginary part [87].

Figure 13. Airfoil attached to piezoelectric cantilever beam with pinned base [87].

If simply harmonic motion is assumed, then the following equation can often be used to solve the flutter equation of motion for an airfoil [100]:

$$[M_{hh}p^2 + (B_{hh} - \frac{\rho cVQ^I_{hh}}{4k})p + (K_{hh} - \frac{\rho V^2 Q^R_{hh}}{2})\{u_h\}] = 0 \qquad (12)$$

where M_{hh} is modal mass matrix, B_{hh} is modal damping matrix, K_{hh} is modal stiffness matrix, $Q^I{}_{hh}$ is generalized aerodynamic damping matrix, $Q^R{}_{hh}$ is aerodynamic stiffness matrix, ρ is air density, c is mean aerodynamic chord length, V is airspeed, $k = \omega c/2V$ – reduced frequency, ω is circular frequency, p is $i\omega$, and u_h is modal displacements.

In another study a linearized analytical model is derived which includes the effects of the three-way coupling between the structural, aerodynamic, and electrical aspects of the system. This all contributes to calculations of the wind speed and frequency at the onset of flutter instability. It was determined that a minimum "cut-in" airspeed was needed for the system to operate and such a parameter would need to be taken into design considerations before further system performance characteristics could be tuned to work in the operating range. System nonlinearities are considered in another study as well as linear flutter speed with the particular

system achieving 10.7 mW of power output [101]. In addition to the vibrations from fluttering, airfoil systems subject to combined loading with base excitations have also been investigated [102]. Figure 14 is a system model illustrating the various aspects of this system, which is similar to other airfoil system models.

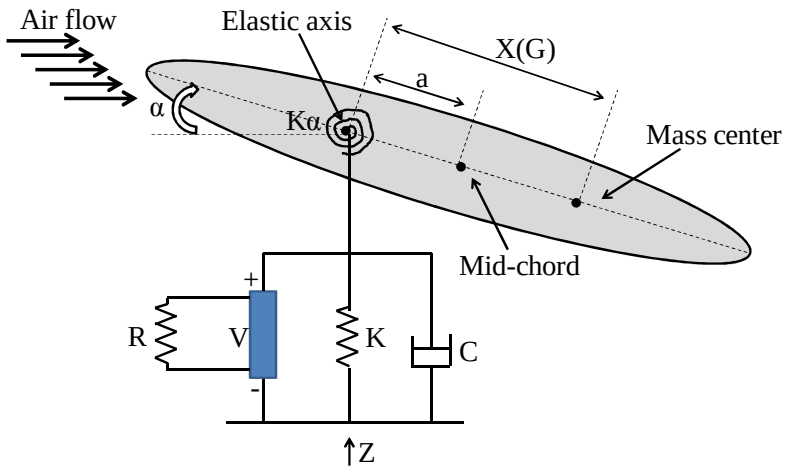

Figure 14. Schematic diagram of airfoil energy harvester [102].

Perhaps, unsurprisingly, the output of the harvester is most improved when base excitation frequency matches fluttering frequency. Another consideration though is the base excitations introduced into the host structure from the energy harvester itself [103]. Depending on the nature and size of the host structure any base excitations introduced through the action of the harvester could prove to be severely detrimental through the very same principles upon which the harvester generates energy.

Yet another method of fluid based energy harvesting is the galloping phenomenon. Galloping is an aero-eleastic instability similar to flutter but distinguished by low frequency,

large amplitude oscillations of the structure when the direction of the wind excitation is normal to the oscillations [104]. Den Hartog explained the phenomenon for the first time in 1934 and developed a criterion for galloping stability based on specified lift and drag coefficients call the Hartog Factor shown in Equation (13)

$$H(\alpha) = \left(\frac{dC_l}{d\alpha} + C_d \right) \rangle 0 \tag{13}$$

where Cl and Cd are the sectional lift and drag coefficients, respectively, and α is the sectional angle of attack. Galloping occurs at high angles of attack where the aerodynamic coefficients are highly nonlinear. Therefore, the criterion is evaluated by considering a linearized slope of Cl versus α at the equilibrium point about which oscillations occur. Galloping onset is characterized by a negative effective damping of the system and corresponding exponential increase in the amplitude of motion with time. However, the system reaches a limit cycle oscillation in a short period of time, after which the amplitude of oscillation remains constant [105]. Galloping-based systems have been shown to develop as much as 50 mW at wind speeds as low as 11.6 mph [105]. The system schematic for such a system is shown in Figure 15. This approach not only produced more output power than certain flutter designs but also has a lower required air speed. However, there were discrepancies between calculated and experimental, magnitudes and natural frequencies, as well as significant power reductions in the event of high wind velocities. This was attributed to the mass effects of the air and air turbulence. Future works by the author are promised to address these concerns in addition to other concerns such as fatigue life of the device. In another study similar to the optimization of bluff bodies previously mentioned [93], recent investigations into the optimization of bluff bodies for galloping based harvesters have

been investigated as well [106]. The square shape was assumed to be the optimal bluff body shape therefore no other bluff body shapes were investigated in this study.

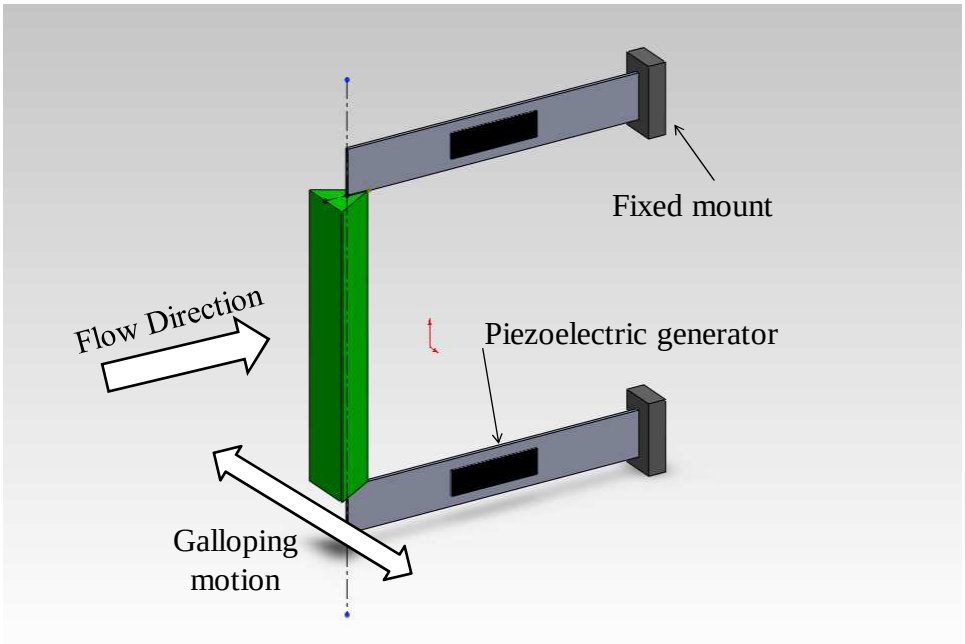

Figure 15. Schematic for galloping based energy harvester [105].

By varying mass, length, and other parameters a maximum output of 8.4 mW was achieved at 8 m/s wind speed. It would be interesting to see the effects of different bluff body shapes on the system as well.

CHAPTER 5

NUMERICAL MODELING

In this chapter, a dynamic model of a piezoelectric flag undergoing aerodynamic excitation is performed to predict the mode shapes and natural frequencies. System response in terms of displacement and voltage output is also desired. The proposed flag is a composite of nylon mesh and a PVDF piezoelectric film. There are several authors who have approached this problem, but their approaches differ in varying degrees, in part because their motivations are different. While many authors model the flag and piezoelectric material separately, this study looks at the combination of the two using Hamilton's principle. With Hamilton's principle it is possible to take these two problems and evaluate them in a way that will give the overall relationship of the system.

5.1 Flag Assumptions

Often the system is approached by modeling the flag as a cantilevered flexible plate under ideal flow [107-109]. However, the flag can also be modeled as a thin membrane [110] . This assumption imposes a different approach to how the internal forces are treated in the flag. Since the majority of authors model the flag as a simple plate/beam with a low bending rigidity, and such an approach has yielded palatable results, that same assumption has been taken in this study. Within the physical mechanics of the flag, many authors agree that the flag can be assumed inextensible [110, 111]. Most studies also agree that the fluid may be modeled as inviscid and incompressible [112].

Some authors assume a flag pinned in the corners or the leading edge with a free trailing edge [110]. While this is a more accurate assumption for flags hung as ornamentation, this assumption does not accurately represent the physical system being modeled in this study. Here, it is assumed that the flag is under clamped-free boundary conditions, which is an assumption agreed upon by many authors. The flag is often regarded as a two dimensional deformation [109, 113], as long as it is within a certain dimensional constraint as a thickness less than 0.028 mm. As a beam, the flag can be modeled using the Euler-Bernoulli beam theory given the sufficiently narrow cross section.

The internal tension within the flag most contested variable of the flag modeling. While most studies treat the flag as a beam, some account for tension in two separate terms: once with respect to the spatial second derivative of the oscillation, and once as with respect to the change in position [108, 111]. Other studies treat tension as a singular value, which can be represented as half the square of the time average velocity. In many cases, tension due to gravity can be neglected [114]. In this study tension is incorporated as a singular value.

5.2 Piezoelectric Assumptions

PVDF was chosen as the piezoelectric material due to its many unique properties among piezoelectric materials. Compared to other piezoelectric materials PVDFs have very low Young's Modulus. This property alone seems to make them ideal for wind-based applications when a flag is the basis for inspiration. PZTs would be far too brittle and even and MFC would be too stiff. While the d31 constant is lower than some other materials this is somewhat offset by the extreme thinness of PVDFs. This thin cross sectional area causes relatively small longitudinal forces to create very large stressed within the material. If the PVDF is laminated then the neutral axis will shift further exploiting this effect. PVDFs also exhibit low moisture sensitivity, low

acoustic impedance, wide frequency range, high impact resistance, high elastic compliance, high voltage output, low thermal conductivity, low dielectric constant, chemical inertness, and can be manufactured in many sizes [115]. Additional material properties are listed in Table 1.

For this system it is assumed that the piezoelectric energy harvester and flag have a 1:1 ratio. It can be readily manufactured in this way and also simplifies the modeling calculations by avoiding heavy-side functions. Additionally, there are no existing studies to suggest any benefits from anything greater than or less than a 1:1 ratio. A system with a ratio greater than 1:1 will be experimentally tested to investigate results in chapter 7. Piezoelectric materials are anisotropic, meaning that they have no center of symmetry [116, 117]. According to some authors, the work done by these materials can be represented as a function of electrical enthalpy density, which is itself a function of the electric field and system constants [118, 119]. This is discussed further in section 5.4.

5.3 Pressure Forcing Term

After considering the flag and the piezoelectric material, to complete the system the pressure difference on the flag must be considered. There are a few different ways to approach this problem. A common approach to flow problems is the Navier-Stokes method. Navier-Stokes equations are based on Newton's second law as it pertains to fluid motion and also assumes that the fluid stress is compiled of the diffusing viscous term and the pressure term. Navier-Stokes can be used in various situations such as weather, ocean currents, water flow in a pipe, and air flow around a wing. The solution to a Navier-Stokes equation is determined by velocity rather than position. When the velocities are found, other variables can be solved for, such as flow rate or drag force. The general form of Navier-Stokes equation is shown below [120].

$$\rho(\frac{\partial v}{\partial t} + v * \nabla v) = -\nabla p + \nabla * T + f \tag{14}$$

where ρ is the fluid density, v is the flow velocity, ∇ is the del operator, p is the pressure, T is the stress tensor, and f is the body forces. In Yadykin's paper, he represented the pressure difference with the slender wing theory as shown below [121]:

$$\Delta p = M(\frac{\partial}{\partial t} + U\frac{\partial}{\partial s})^2 h(s,t) \tag{15}$$

where M is the added mass represented by the equation below, U uniform and constant velocity of flow, and h is the deflections of the material.

$$M = \frac{\rho \pi H}{4} \tag{16}$$

where ρ is the density and H is the width. For potential flow, Moretti uses a simplified approach with the effective mass of air acting on the system [108, 111, 114]:

$$\Delta p = -(m_a \frac{\partial^2 w}{\partial t^2} + 2m_a U_\infty \frac{\partial^2 w}{\partial t \partial x} + m_a U_\infty^2 \frac{\partial^2 w}{\partial x^2}) \tag{17}$$

where m_a is the effective mass represented by the equation below for slender flags, w is the deflection in the z-direction, U_∞ is the free stream velocity, and x is the distance along the initial plane of the flag.

$$m_a = \frac{\pi \rho_{air} d}{4} \tag{18}$$

where ρ_{air} is the density of air and d is the width. To further simplify this equation we can use the relationship below for slender flags [108]:

$$m_a U_\infty^2 = \frac{2}{3}\left(\frac{m}{2} * \frac{A^2 w^2}{2}\right) \quad (19)$$

Where A is the maximum amplitude and m is the mass of the flag.

5.4 Modeling

Piezoelectric materials create electric energy based on the ability to convert an input strain (displacement) into an electrical response. Some piezoelectric material work better at low frequency than high frequency and vice versa [37]. For our project we consider a PVDF thin-film piezoelectric energy harvester coupled to a flag. The piezoelectric material for the flag is bound by the constitutive equations as follows:

$$D = \varepsilon^T E + d_{31} T \quad (20)$$

$$S = d_{31} E + s^E T \quad (21)$$

These are the same constitutive equations presented in Ch.2 via Equations 1 and 2. In this particular system the piezoelectric constant has a subscript of 31 which represents two distinct characteristics. The first three notates the direction of poling and the second number is the direction of the electric field. For our study the three direction is parallel to the length of the flag. It is important to note that for a one-dimensional piezoelectric material the deflections in the other direction will have little to no effect for the sensing of the system [122]. Likewise, the actuation will mainly affect the system in the direction of the piezoelectric material when a current is applied to the system.

The next step of modeling a piezoelectric material is to consider the electric enthalpy of the system. The electric enthalpy of the system is considered as a potential term. The process to derive this term starts with discrete piezoelectric transducer. The equation for the net work of the transducer is shown below [116, 117]:

$$dW = Vidt + f\dot{\Delta}dt = VdQ + fd\Delta \tag{22}$$

where dW is the net work, Vi is the electric power, $f\dot{\Delta}$ is the mechanical power, and Q is the total electric charge of the electrodes of the transducer, Δ is the total extension. The net work will be converted into stored energy for a conservative element. After integration the equation below is found:

$$dW_e(\Delta, Q) = \frac{\partial W_e}{\partial \Delta} d\Delta + \frac{\partial W_e}{\partial Q} dQ \tag{23}$$

Integrating the above equation gives

$$W_e(\Delta, Q) = \frac{Q^2}{2C(1-k^2)} - \frac{nd_{33}K_a}{C(1-k^2)} Q\Delta + \frac{K_a}{1-k^2}\frac{\Delta^2}{2} \tag{24}$$

where K_a is the stiffness with a short-circuited electrode, C is the capacitance of the transducer, and n is the number of piezoelectric material stacks. Then the total differential of the coenergy is represented by:

$$W_e^*(\Delta, V) = VQ - W_e(\Delta, V) \tag{25}$$

By taking the differential, introducing the constitutive equations and then integrating, the final equation is shown as

$$W_e^*(\Delta,V) = C(1-k^2)\frac{V^2}{2} + nd_{33}K_aV\Delta - K_a\frac{\Delta^2}{2} \tag{26}$$

where the first term on the right side of the equation represents the electric coenergy, the second term is the piezoelectric coenergy, and the third term is the strain energy stored in a spring of stiffness K_a which corresponds to short circuited electrodes [116, 117]. Another way to represent this equation is:

$$-H = W_e^* = \int_0^l A(\frac{1}{2}\varepsilon_{33}^S E_3^2 + S_1 e_{31} E_3 - \frac{1}{2}c_{11}^E S_1^2)dx \tag{27}$$

where A is the cross-sectional area, c is the elastic stiffness under a constant electric field, e_{31} is the piezoelectric stress constant, E_3 is the electric field in the three direction, and S_1 is the strain along the axis of the bar. For a flag system the length of the piezoelectric material is greater than the thickness. This will allow the first term to be neglected due to it being relatively small [121].

5.5 Equation of Motion

Though the equations of motion for a fluttering flag have been extensively researched, they differ even within separate works by the same author [108]. The motion of a flag can be described similarly to that of a web [123]. Most authors agree on some form of the following equation [124]:

$$m_{flag}\frac{\partial^2\omega}{\partial t^2} - T\frac{\partial^2\omega}{\partial x^2} + EI\frac{\partial^4\omega}{\partial x^4} = \Delta p_{(t,x)} \tag{28}$$

The second part of the equation of motion comes from the addition of the Navier-Stokes stress tensor to the flag surface. Through the constitutive equations, it is possible to model the motion of the piezoelectric material using Hamilton's principle. These constitutive equations form the

basis for the electric enthalpy term $-H = W_e$. These two setups were then paired together and evaluated with Hamilton's Principle to derive a new equation of motion for a piezoelectric material mounted onto a flag.

5.6 Hamilton's Principle

Hamilton's Principle is used in this analysis due to the ability to solve for the system equation of motion and the boundary conditions simultaneously. Some steps in between the following equations are omitted from this chapter due to their extensive nature. Detailed analysis of these steps can be found in the appendix. The general form for a piezoelectric energy harvester is shown below

$$\int_{t1}^{t2} [\delta W_e + \delta T - \delta U] dt = 0 \tag{29}$$

where the electric enthalpy and kinetic energy terms are added and the potential energy term is subtracted. As discussed earlier in this chapter, the individual terms for the system dynamics, piezoelectric dynamics, and pressure term are compiled and evaluated to yield the integrated equation below.

$$m_{flag} \frac{\partial^2 u}{\partial t^2} + EI \frac{\partial^4 u}{dx^4} - (T(x) \frac{\partial^2 u}{\partial t^2}) - \frac{\partial^2}{\partial x^2} (e_{31} E_3 b_p h_p z) + (D \frac{\partial^2 u}{\partial^2 x}) = \Delta pz \tag{30}$$

The boundary conditions are simultaneously generated along with the integrated equation of motion and are described below

$$u(0) = 0, u'(0) = 0 \tag{31}$$

$$(e_{31} E_3 b_p hz + Du'') \delta u' \Big|_0^L = 0 \tag{32}$$

$$((e_{31}E_3 b_p hz)' + (Du'')')\delta u\Big|_0^L = 0 \tag{33}$$

where Equation 31 shows the displacement and slope at x=0, and Equations show 32 and 33the moment and force of the system evaluated at x=0 and x=L. Moment and force at x=0 are both zero.

CHAPTER 6

ANALYTICAL RESPONSE

The equations of motion for different dynamic systems have been evaluated in the time and frequency domain, using eigenvalue analysis, assumed mode method, or time-marching with either the generalized coordinates or the Navier-Stokes code [120]. The equation of motion can also be evaluated using the Rayleigh-Ritz method [119]. Here, the system parameters are separated using Galerkin method. The mode shapes are used to evaluate the response of the system.

6.1 Modal Analysis

Once the equation of motion and the boundary conditions are found then modal analysis of the system to gain to modes shapes can begin. The first step in this process is the separation of variables. This is done assuming system response is separable into its spatial and time components represented by u(x,t)=ϕ(x)q(t). The assumed form of the general solution can then be represented by

$$\phi(x) = C_1 \sin(\beta x) + C_2 \cos(\beta x) + C_3 \sinh(\beta x) + C_4 \cosh(\beta x) \tag{34}$$

where the C_n coefficients can then be solved by reconsidering the boundary conditions and plugging them in. Equation (34) is the general solution for the mode shape of Equation (30). However, this mode shape does not satisfy the boundary conditions presented in Equations (31-33); therefore, a modified comparison function is introduced in the following equation as the mode shape of the system which considers the effect of piezoelectric electromechanical coupling at boundary conditions

$$\Psi(x) = \Phi(x) + PVDF[\int\int \Phi dx dx]\frac{1}{6}(\frac{x}{l})^3 \tag{35}$$

where

$$PVDF = \left[\frac{e_{31}bz}{D} * \frac{bh}{\sqrt{2}d_{31}L^2}\right] \tag{36}$$

This PVDF term represents the spatial component of the piezoelectric energy harvester to the system. Through the boundary conditions, the relationships of C1 = -C3 and C2 = -C4, can be made from Equation (35). A new variable R was then used to simplify the relationship and MATLAB code

$$R = \frac{C_4}{C_3} = \left[\frac{(\cosh(\beta L) + \cos(\beta L)) - (\sinh(\beta L) + \sin(\beta L))}{\beta(\cosh(\beta L) + \cos(\beta L)) - \beta(\sinh(\beta L) - \sin(\beta L))}\right] \tag{37}$$

The beta values needed to solve for variable R cannot be solved explicitly. Rather an implicit solution through graphing is achieved. This graph is depicted in section 6.3 of this study and generated from the following

$$\beta^4 = \frac{\rho\omega^2}{EI + D} \tag{38}$$

With these terms, it was then possible to explicitly solve for the first mode shape

$$\Psi(x) = C\frac{PVDFx^3}{6L^3\beta^4}[(\sin(\beta x) + \sinh(\beta x)) + R(\cos(\beta x) + \cosh(\beta x))] + \sin(\beta x) + \sinh(\beta x) + \cos(\beta x) - \cosh(\beta x) \tag{39}$$

where C is a constant that can be normalized by the equation shown below.

$$C = \sqrt{\frac{1}{\int_0^L \rho \Psi^2 dx}} \tag{40}$$

"C" is found inside Ψ, and is factored out of the integral.

6.2 Response Through Galerkin Method

The Galerkin method is an approximate method that allows for the solution of the ordinary differential equation while satisfying all boundary conditions. The generalized form of the Galerkin method is as follows

$$u(x,t) = \sum_{n=1} \psi_n(x) q_n(t) \tag{41}$$

where Ψ_n and q_n represent the adjusted spatial function and the time function respectively. Transforming the equation of motion into Galerkin form yields the following equation

$$\left(\rho\omega^2\right)\Psi\ddot{q} + \left(EI + D\right)\Psi'''q = m_a\Psi\ddot{q} + 2m_a u_\infty \Psi'\dot{q} + m_a u_\infty^2 \Psi'' q \tag{42}$$

which can be further simplified to the following form:

$$M_s\ddot{q} + K_s q = M_a\ddot{q} + C_a\dot{q} + K_a q \tag{43}$$

Having found Ψ in the previous section it is now necessary to find q. Combining like terms we can then take the Laplace of the next equation:

$$£\{M\ddot{q} + C\dot{q} + Kq\} = 0 \tag{44}$$

Evaluating the previous equation, q is solved for in two ways; with damping C and then without. This q term represents the time solution allowing the full response to now be solved.

$$q1 = -M\omega\left[\frac{e^{t\left(-\frac{\sqrt{C^2-4KM}}{2M}-\frac{C}{2M}\right)} - e^{t\left(\frac{\sqrt{C^2-4KM}}{2M}-\frac{C}{2M}\right)}}{\sqrt{C^2-4KM}}\right] \tag{45}$$

$$q2 = \frac{\omega\sin\left(\sqrt{\frac{K}{M}}t\right)\sqrt{M}}{\sqrt{K}} \tag{46}$$

Then the K term is evaluated through integration-by-parts. Once q is found via the Laplace transform it can be combined with Ψ to create the function u(x,t) which is our desired response. Voltage output can also be derived based on the EOM and system response and is shown below [125]

$$V = \frac{bh_p}{d_{31}L^2\sqrt{2}}u \tag{47}$$

6.3 Modeling Results

The beta value first introduced in the last chapter was solved implicitly through plotting as shown in the Figure 16 where beta is equal to 10.36. Using the equation for beta shown earlier, ω is found to be 9.96 rad/s.

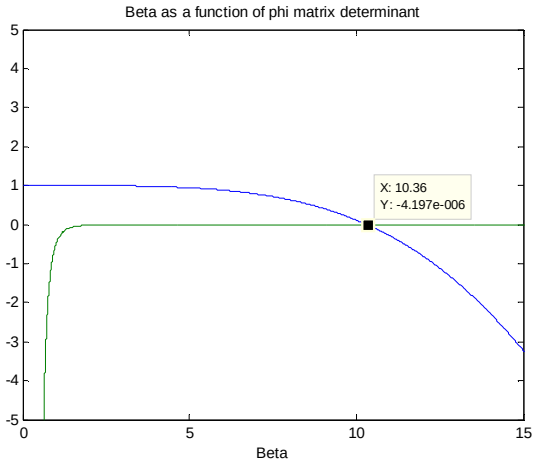

Figure 16. Implicit solution for beta value.

Once a beta value has been determined implicitly it can be used to solve for system response. MATLAB was utilized in most of the data analysis and figure generation. Figure 17 shows the undamped system response with the implicit beta value, Figure 18 shows the oscillating voltages versus time at any value of x, and Figure 19 shows the undamped voltage response versus time.

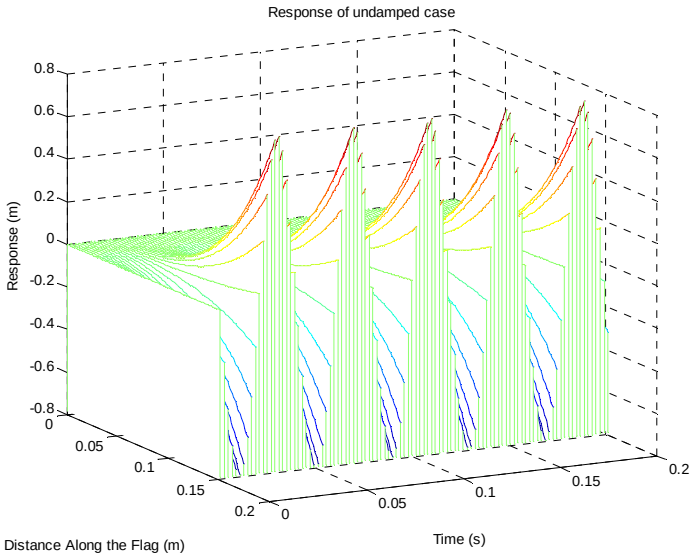

Figure 17. Undamped system response versus time and flag position x.

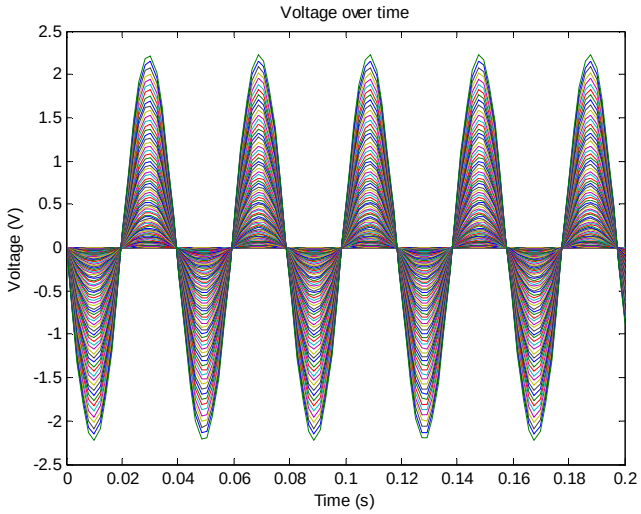

Figure 18. Voltage at any discrete point x.

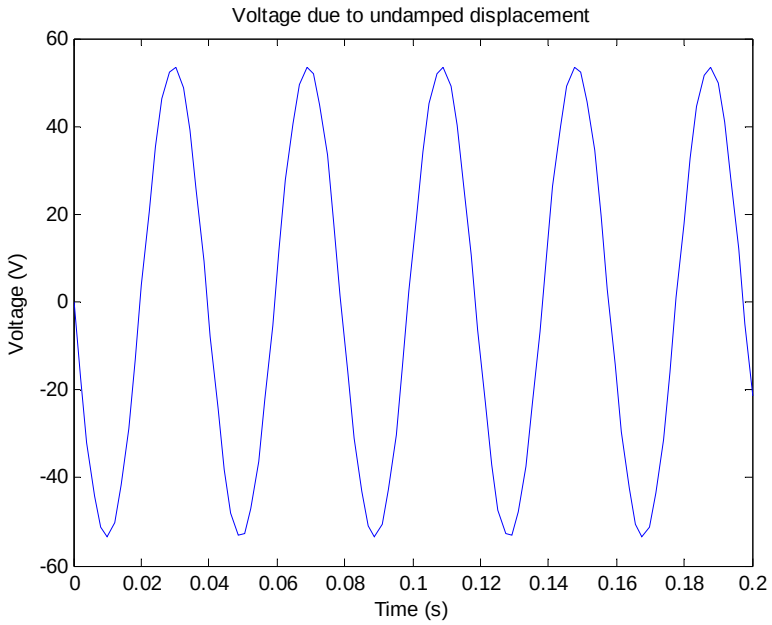

Figure 19. Undamped voltage response vs. time.

Based on the fundamental period, the frequency of oscillation for the undamped case is calculated to be 26 Hz. Notice that due to the lack of damping, this response has a constant

maximum amplitude throughout the duration of the sample. System damping from mechanical, electrical, and aerodynamic effects were intentional omitted from this analysis to allow for a more straight forward approach. The introduction of these terms will yield more accurate system modeling but will greatly complicate the analytical computations. Likewise, alternate forms of both pressure terms and flag EOMs exist as discussed in each section of this chapter. Different analytical techniques will no doubt yield different results but it is not within the scope of this study to compare one analysis method to another. The analytical results (frequency response) from this chapter however will be compared to the experimental results generated in the following chapter.

CHAPTER 7

EXPERIMENTAL TESTING

In this chapter experimental methods and results from flag-based piezoelectric energy harvesters are presented. The purpose of these tests is to investigate the validity of the results from previous chapters as well as gain additional insight into these systems and provide vision for future studies.

7.1 Material Selection

Two types of piezoelectric materials were chosen for testing. PVDF was chosen due to the properties explained in Chapter 5 and the Macro Fiber Composite (MFC) was chosen as a comparison material for wind energy harvesting since MFC is more flexible than other PZT materials. The PVDFs were sourced from Images Scientific Instruments. They are of the piezoelectric film type and carry part numbers PZ-02 and PZ-04 respectively. The MFC by construction is a matrix of piezoelectric ceramic rods suspended between layers of adhesive (epoxy), electrodes, and polyimide film. Invented in 1996 by NASA they are now licensed and manufactured by Smart Material Inc. [126]. MFCs were chosen as a comparison material mainly due to the fact that it is the only other piezoelectric material currently on the market that offers moderate levels of flexibility. According to Smart Materials, MFCs are excellent at harvesting energy from vibrations, available in single crystal form, flexible, durable, reliable, come in various sizes, environmentally sealed, damage tolerant, and able to operate in d33 or d31 modes [126]. The MFCs tested are product number M2814P2 and M8557P2. For all of these reasons it becomes clear that the MFC is currently the most similar piezoelectric material on the market to the PVDF film based sensors. Table 1 below shows a comparison between material properties.

Table 1. Piezoelectric Material Properties

Property	PZ-02	PZ-04	M2814-P2	M8557-P2
Area (cm^2)	6.56	115.5	6.66	64.1
Volume(cm^3)	0.131	0.693	0.199	1.92
Capacitance (nF)	2.45	43.9	25.7	402
d31 (pC/N)	23	23	210	210
e31 (mVm/N)	216	216	NA	NA
Young's Modulus (GPA)	2-4	2-4	30.3	30.3

From Table 1 it is shown that there are two sample sizes for both PVDFs and MFCs. Material size was chosen so that both "large" and "small" sizes are similar between material types. Two material properties that stand out are the d31 constant and Young's Modulus. The MFCs have a much higher d31 constant indicating that they are more efficient and should yield a higher electrical output for a given mechanical input than the PVDFs. However, the PVDFs have a significantly lower Young's Modulus indicating that the materials are far more flexible than the MFCs. Given the desire for a flag-like membrane the lower modulus of the PVDFs may yield higher levels of deflection and therefore higher voltage outputs for a given mechanical input despite the lower d31 value.

7.2 Experimental Procedure

The materials discussed in 7.1 were subjected to a variety of wind velocities while measuring voltage output. To achieve this, initial tests were conducted on a table top set up shown in Figure 20.

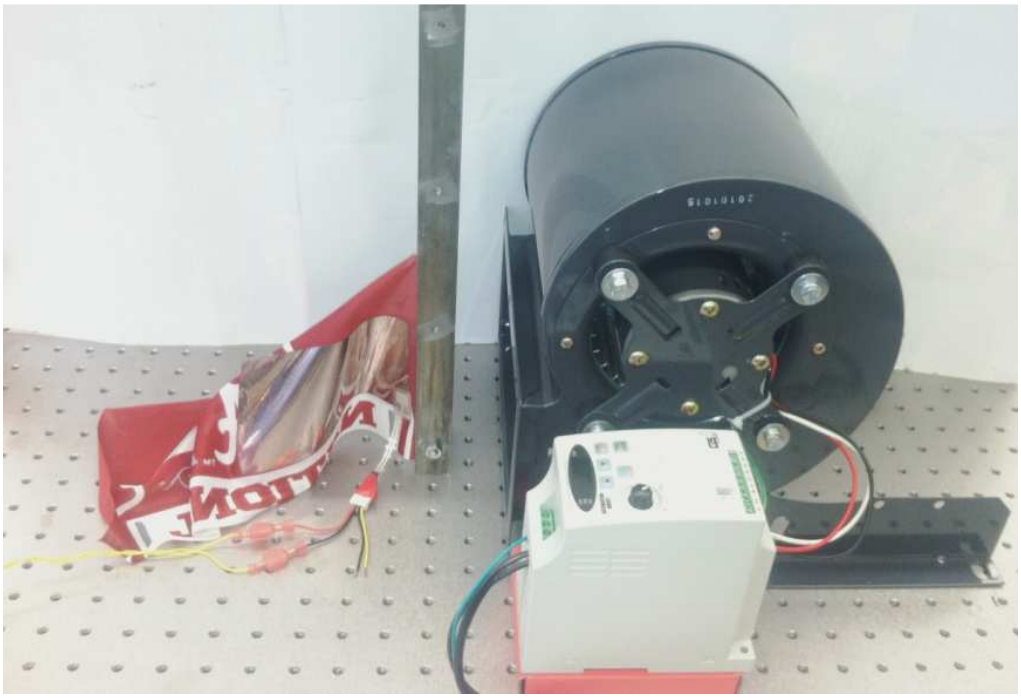

Figure 20. Table top piezoelectric energy harvesting flag test.

Initial equipment included a flag stand machined from 0.5'' mild steel, a centrifugal AC fan, an Automation Direct Variable Frequency AC Drive to control the fan, a Fisher Scientific Hot Wire Anemometer, Tektronic TDS-2004C oscilloscope, and Thor optic tables. These initial tests were done with the full understanding that flow would not be steady state or laminar. The purpose of these preliminary tests was to observe electrical and mechanical system behavior prior to full wind tunnel tests. Several things were observed: Electrical noise was a constant source of problems with data collection. Given the low energy output typical of piezoelectric energy harvesting systems even the 60Hz electromagnetic interference (EMI) from power sources in the

room could be an issue. Further testing confirmed the analytical results from Ch.6 that we would be operating at frequencies <100Hz. This also caused issue from the 60Hz noise. To mitigate these issues we employed the use of several noise canceling techniques. EMI shielding sleeves, shielding magnets, and rubber isolators were purchased from McMaster Carr. The magnets and sleeves were installed in-line on the oscilloscope BNC cables while the rubber isolators were installed as additional grounding measures on the flag stand. These measures limited noise saturation but by nature PVDF are susceptible to EMI. The additional use of signal conditioning and post data collection filtering was considered but ultimately never needed. This was due to the lack of noise once the tests were moved to the low-speed wind tunnel. Noise was only an issue in the table top experiments.

Once satisfactory methods were developed in laboratory, the test was moved to the low speed wind tunnel housed in Hardaway Hall on campus. This wind tunnel is manufactured by Aerovent and provides steady state, laminar airflow in the range of 1 - 45+mph. Wind tunnel velocity measurements were provided by in tunnel pitot-static tubes connect to dedicated National Instruments data acquisition hardware and a computer with LabVIEW software. The same Tektronix oscilloscope was used to gather and analysis voltage data, while a new flag mount was fabricated to mount to the wind tunnel. Pictures of the wind tunnel can below in Figures 21 and 22.

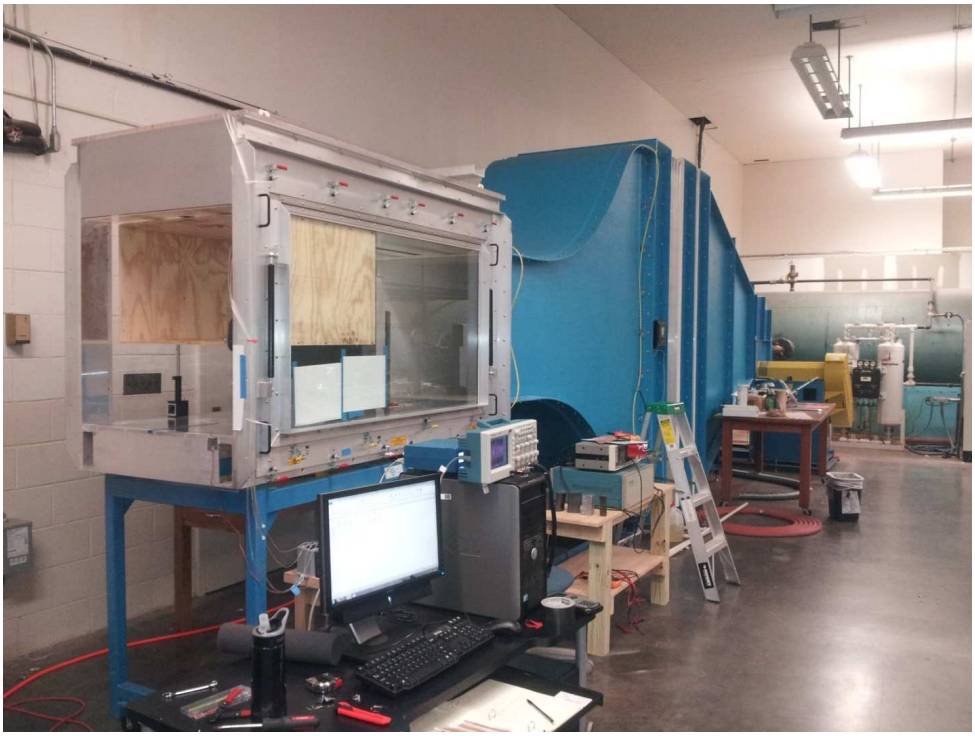

Figure 21. Low speed wind tunnel lab.

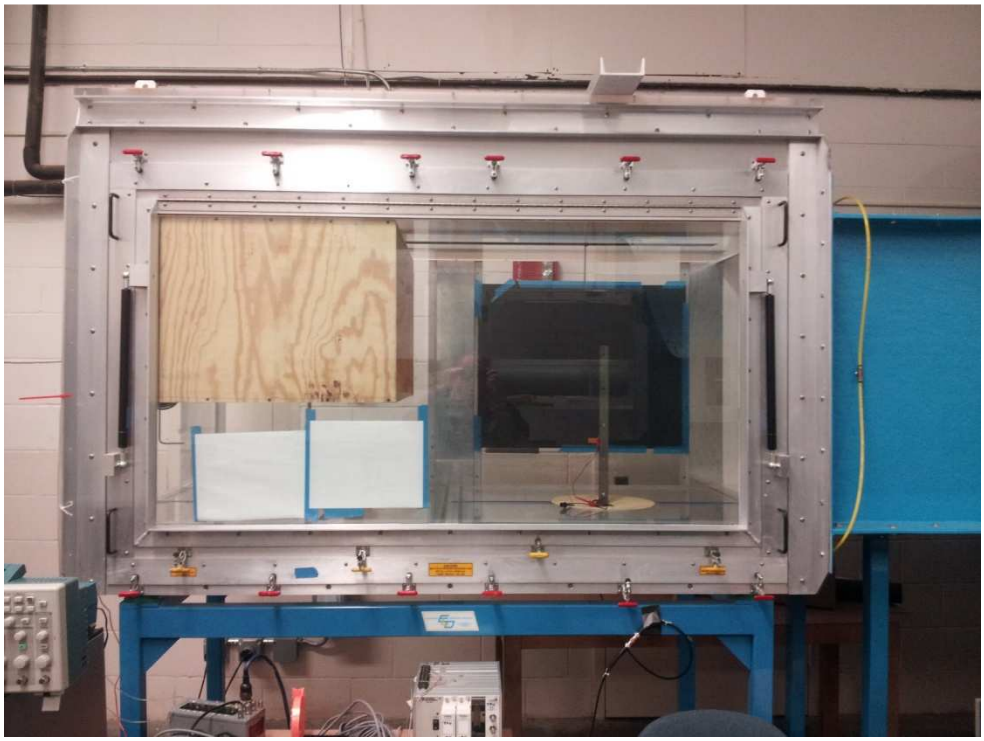

Figure 22. Test cell with energy harvester installed.

The tests conducted were done in the interest of voltage output versus time. To accomplish this various wind velocities, measured in mph, were tested. The PVDFs and MFCs were tested in their stock configuration as well as in modified forms. These modifications included the addition of larger flag or tail sections, as well as the introduction of bluff bodies to alter vortex generation. The bluff bodies will be discussed later in this chapter. Figure 23 shows the PZ-02 PVDF on the left in stock configuration as well as with a nylon tail section attached via epoxy. The large and small harvesters on the right are the M8557-P2 and M2814-P2 MFCs respectively. A quarter is pictured for scaling purposes. Figure 24 shows the PZ-04 PVDFs with nylon flag backing. In the upper harvester the flag to harvester ratio is >1. This is to test if additional flag area leads to additional harvester motion. This will be referenced as PVDF w/ Flag for the rest of the study. The lower harvester has a 1:1 flag to harvester ratio and is representative of the system modeled in Ch.5. Once again a quarter is pictured to offer a scaling reference.

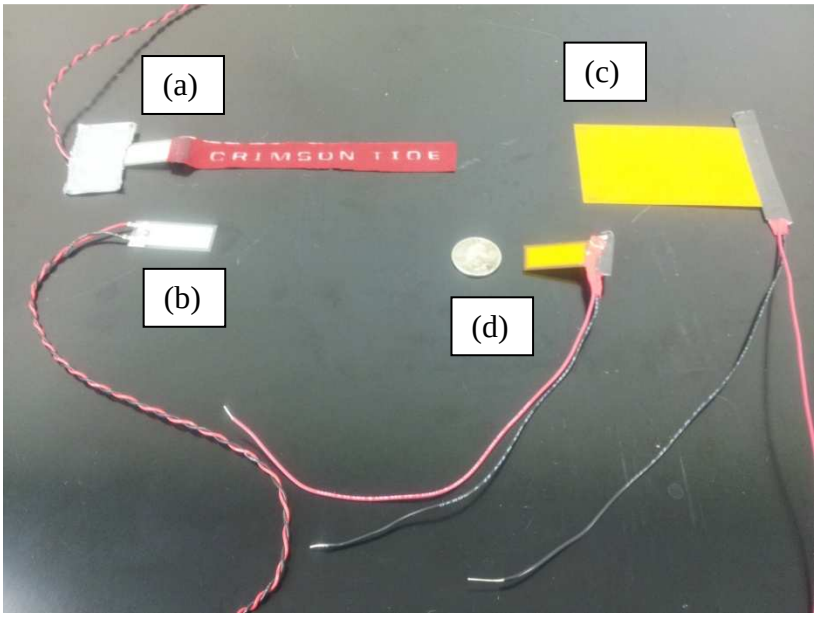

Figure 23. (a)PZ-02 w/ tail section (b) PZ-02, (c) M8557-P2, and (d) M2814-P2.

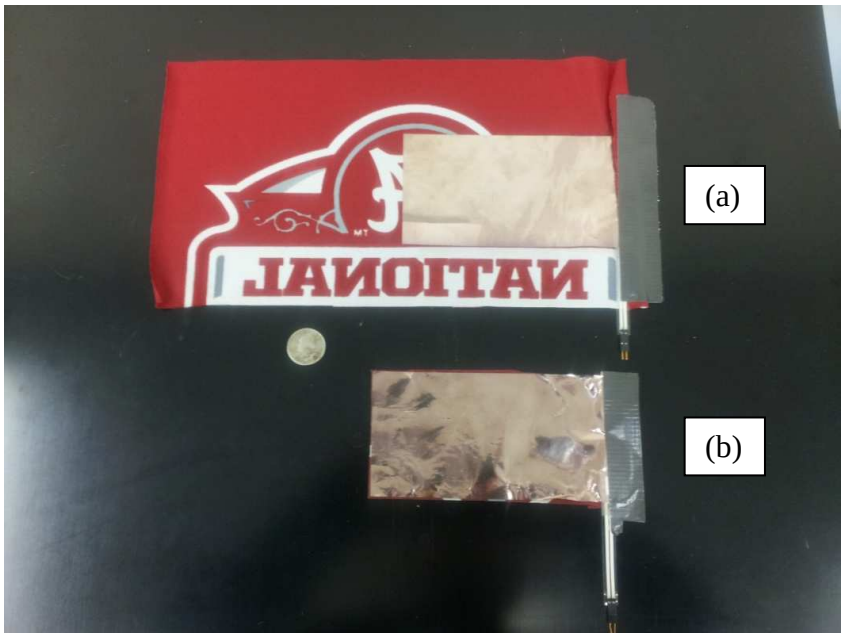

Figure 24. (a) PZ-04 w/flag body, (b) PZ-04 with 1:1 flag to harvester ratio.

All piezoelectric materials were clamped in a similar manner yielding clamped-free-free-free end conditions. All materials were subjected to the same 5-35 mph wind speeds. Thirty-five miles-per-hour was chosen as the highest test speed due to observable damage taking place on the PZ-04 PVDF harvesters at speeds approaching 30-35 mph. Additionally, while an end use application is not in the scope of this project, it is logical to assume that wind speeds in excess of 35 mph will most likely have limited use in practice.

7.3 Experimental Results

The results presented in the following two sections were generated from data collected over several weeks of wind tunnel testing and up to 800 individual runs performed. To harvest the voltage generated from the harvesters, the oscilloscope is connected directly to harvester. This acts as a pure resistance of 1M Ohms. Resistive loads and conditioning circuits can be incorporated depending on intended operating bandwidth and results [115]. For the purposes of this study, operational bandwidth is tested throughout the range at a constant load. Data was

gathered for each run and then analyzed individually. An example of a harvester output can be seen in Figure 25.

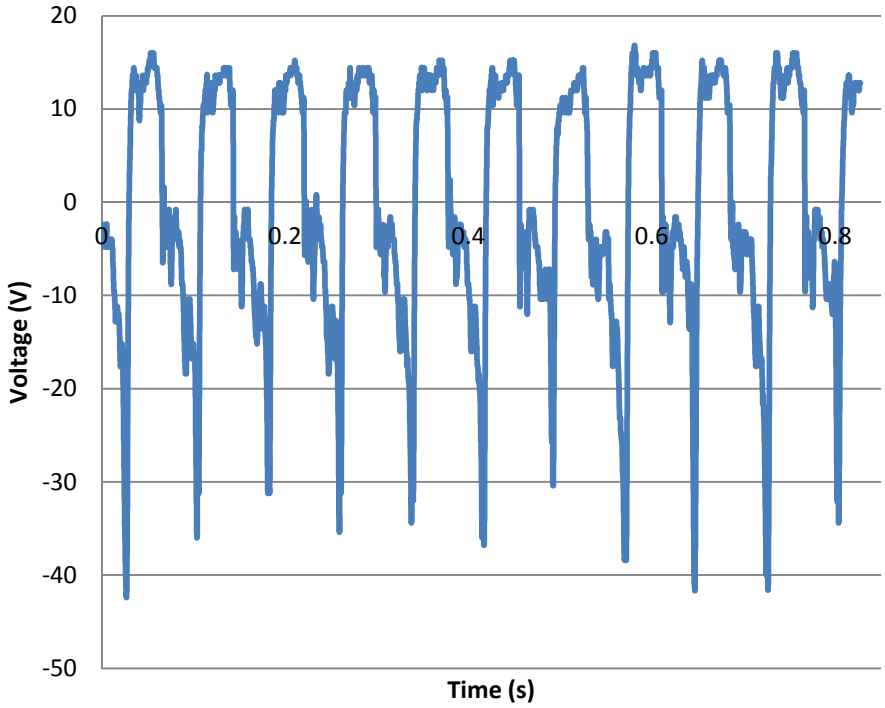

Figure 25. Typical measured output from PVDF harvester.

As shown in Figure 25, the PVDF has entered into a periodic motion typical of limit-cycle oscillations induced by vortex shedding. Peak-to-peak voltage, max voltage, average voltage, and Root Mean Square (RMS) voltage are calculated based on these measurements. The RMS voltage is used to calculate the power produced using the following equation

$$\text{Power} = \frac{(V_{RMS})^2}{R} \tag{48}$$

where V_{RMS} is the RMS voltage and R is the system resistance. In this case the system resistance is the 1 MOhm from the oscilloscope. Data from figures like Figure 25 was also used to calculate operating frequency based off the number of periods for a given time interval. Variations in

operating frequency due to size and material differences were to be expected and are shown in Figure 26. In both cases additional flag material decreased the operating frequency when compared to its flagless counterpart. This decrease was more notable in the case of the MFCs and PZ-02. The operating bandwidth (Hz) of the MFCs is also notably larger than the bandwidth of either PVDF. While the PZ-04 had a operating bandwidth of less than 20Hz between 5 mph to 30 mph, the PZ-02 only had a bandwidth of roughly 10 Hz for the same velocity range. This would suggest that the PZ-02 would be well suited to further efficiency optimizations such as impedance matching. Looking at power output versus velocity offers additional insight into these systems and offers further information about the power produced at various frequencies.

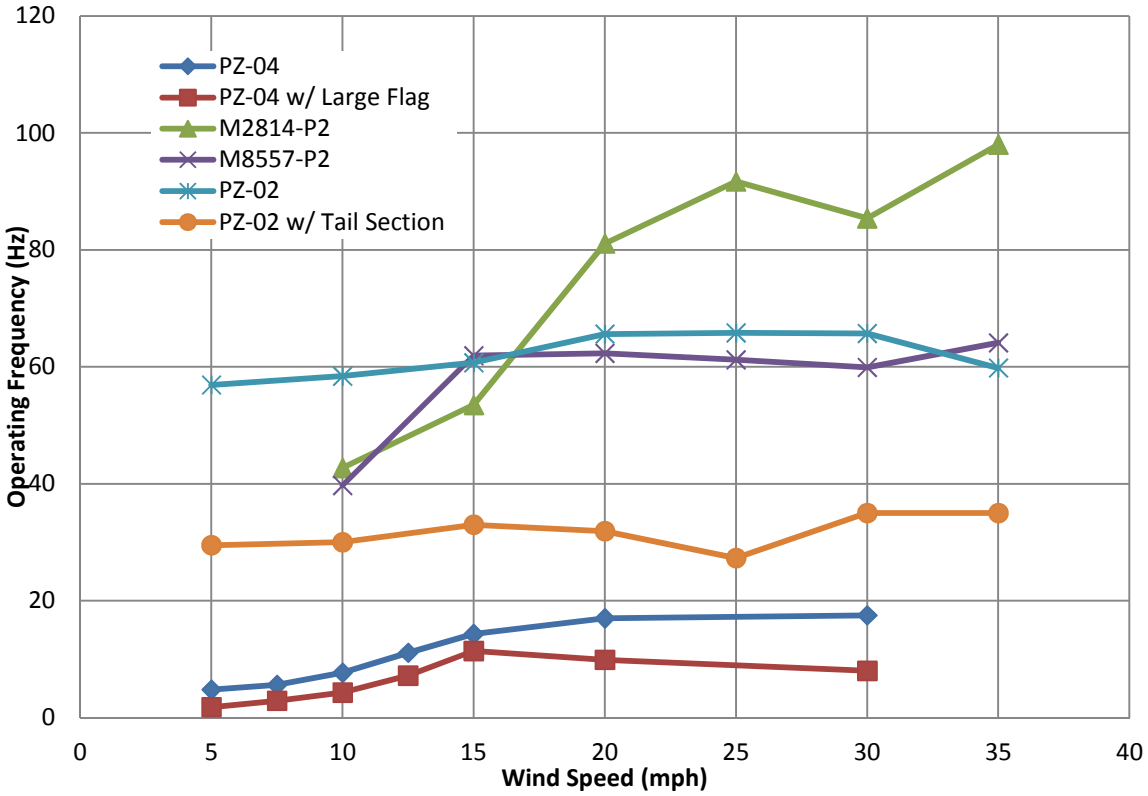

Figure 26. Operating frequency vs. wind speed for all materials.

First let's consider each material independently. Figure 27 shows the power output versus time for the PZ-04 PVDF harvesters. As previously mentioned, the addition of the flag body decreased the operating frequency. In this case it causes a significant reduction in power production. The resulting power outputs are magnitudes apart and the regular PZ-04 is superior at every velocity. There is a sharp increase in power production between 15, 20, and 30 mph. Based on wind tunnel test observations this is most likely due to the flag achieving the lock-in region discussed in Ch.4. A picture of the PVDF experiencing these high amplitude oscillations is shown in Figure 28.

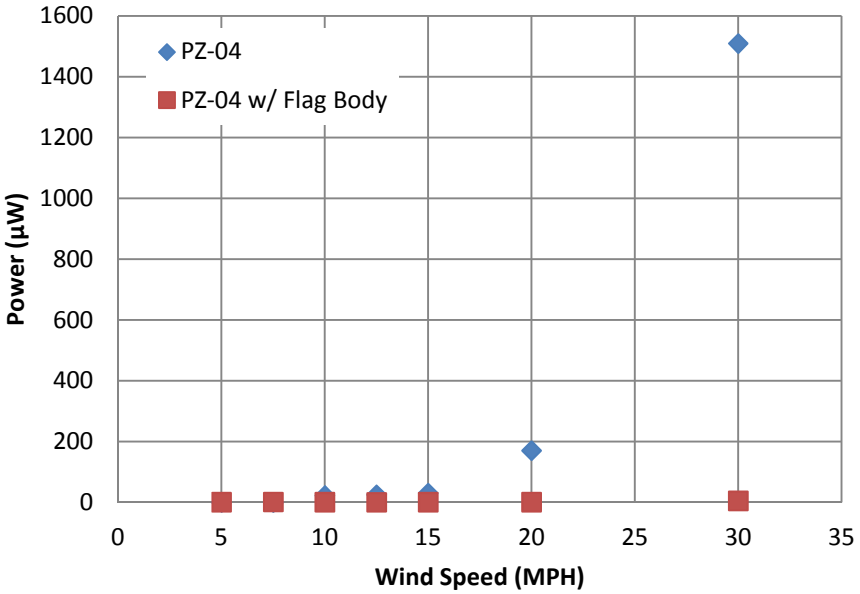

Figure 27. Power output versus velocity for PZ-04 PVDF.

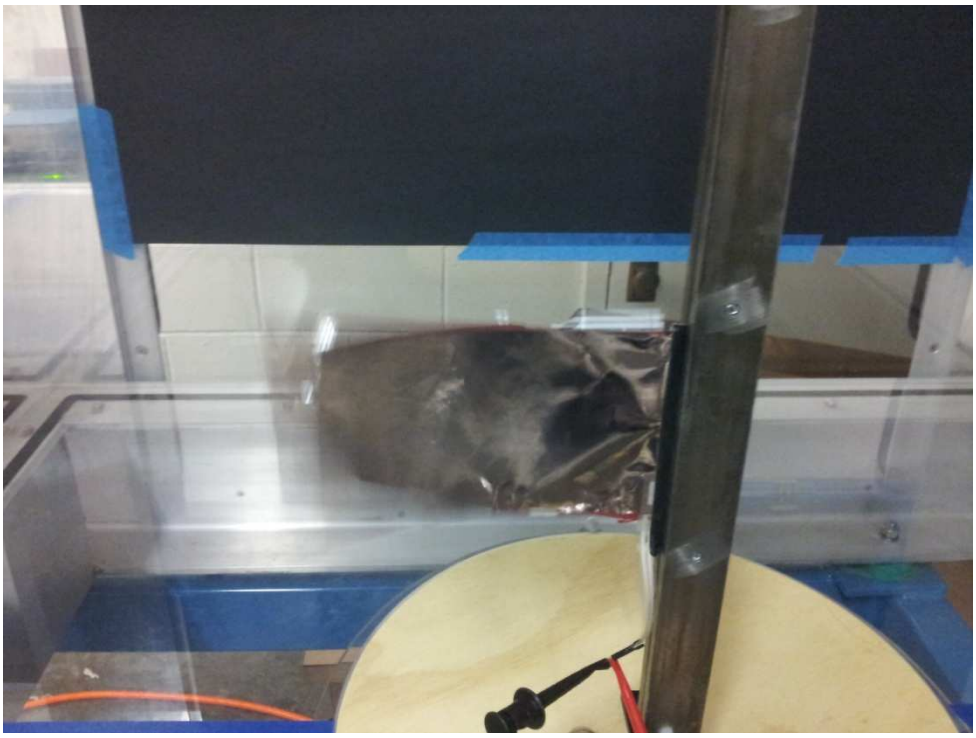

Figure 28. PZ-04 experiencing lock-in.

Next the power output versus velocity is graphed for the smaller PZ-02 PVDF in Figure 29. The PZ-02 shows the same sharp increase in power production at 15mph as the PZ-04. However, it quickly drops off from there rather than increasing perhaps indicating a narrow lock-in range. The addition of a tail section lowers the power production until 35 mph is achieved. In this instance the PZ-02 without a tail section is superior. The maximum power output for the PZ-02 is in the nW range while the PZ-04 was in the mW range.

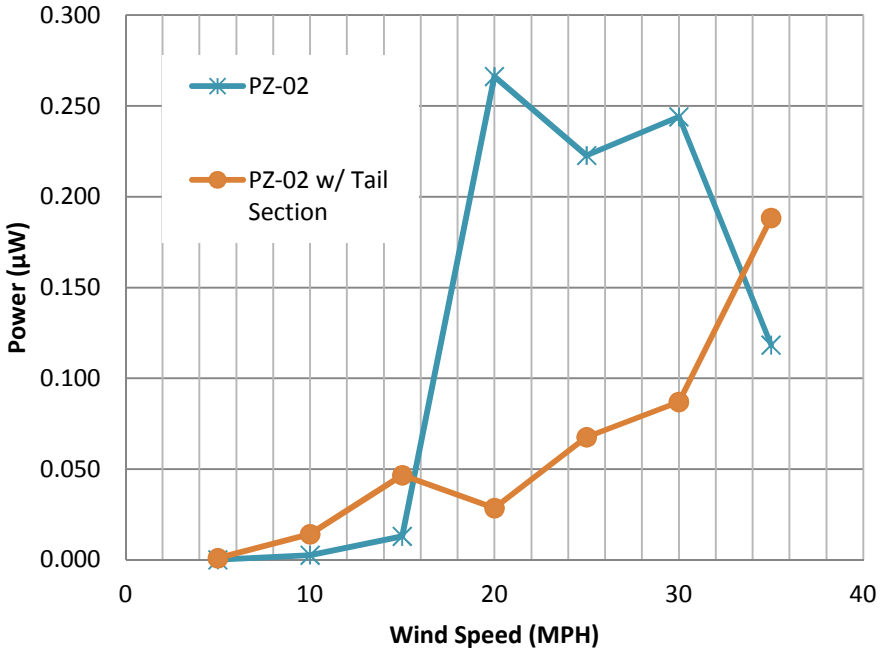

Figure 29. Power output versus velocity for PZ-02.

The MFCs power output versus time data is shown in Figure 30. This output data has dropped another several orders of magnitude down from the previous. Peak power production is now on the pW scale. Once again there is a specific wind velocity that marks a noted power increase followed by a decrease once again indicating a possible lock in region. As expected the larger MFC performed better than the smaller MFC.

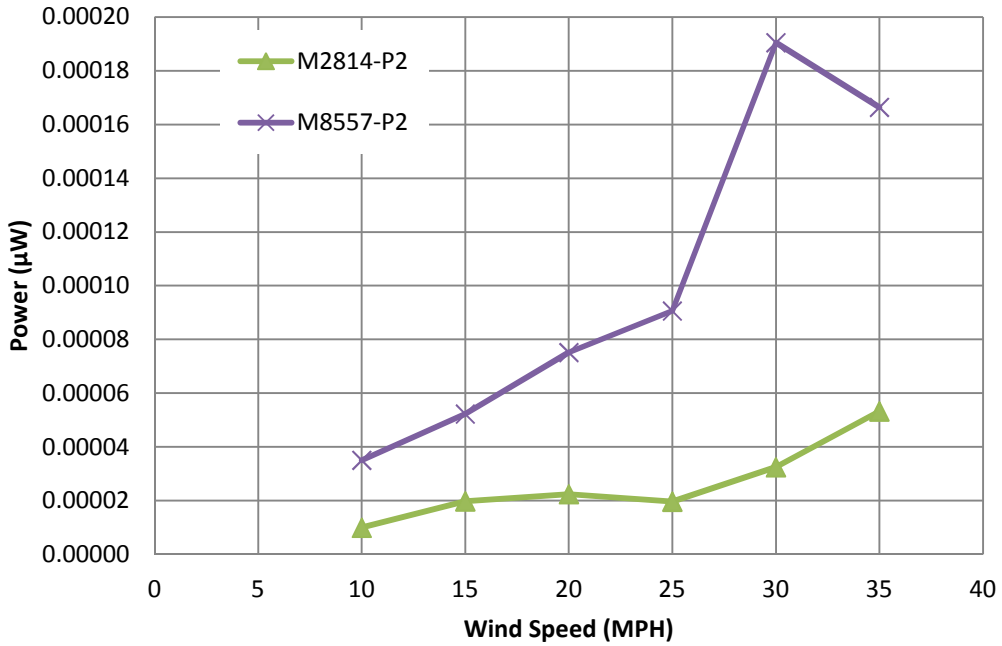

Figure 30. Power output versus velocity for MFCs.

Considering that the power output of the PZ-04 is orders of magnitude greater than any other harvester it is perhaps moot to include a graph including the power output versus velocity for all of the materials overlaid at this point. It can be concluded from the figures discussed in this section that the PZ-04 achieves the highest power output at every velocity tested, and also operates at the lowest frequency.

Throughout testing visible changes began to manifest themselves on the PZ-04 PVDF. These visible changes correlated with a notable decrease in system performance of the PZ-04. A picture of the PZ-04 PVDF is shown in Figure 31. This is not a brand new harvester but one that has sustained some evident damage from numerous tests. It is worth noting that this damage did not occur until wind speeds in excess of 30 mph were tested. At that time, oscillations and deflections became extreme with wrinkles developing from sustained high frequency operation.

This frequency and deflection was on the order of >20Hz, >2 inches, and was sufficient enough to cause plastic deformation. This plastic deformation caused localized stress concentrations in the form of creases which impart a stiffening effect on the harvester. It is possible to overcome these effects with higher wind velocities but further damage to the harvester will likely result.

Figure 31. Plastically deformed PZ-04 PVDF.

Tests were conducted with a new PZ-04 as well as with the damaged one. RMS voltages were calculated, and power was calculated based on Equation 48 for both harvesters. Figure 32 shows the graph comparing power outputs and illustrates the detrimental effects of the plastic deformation. Max power for the damaged harvester is 0.6 μW at 30 mph. No other harvesters exhibited degrading performance due to fatigue or excessive use.

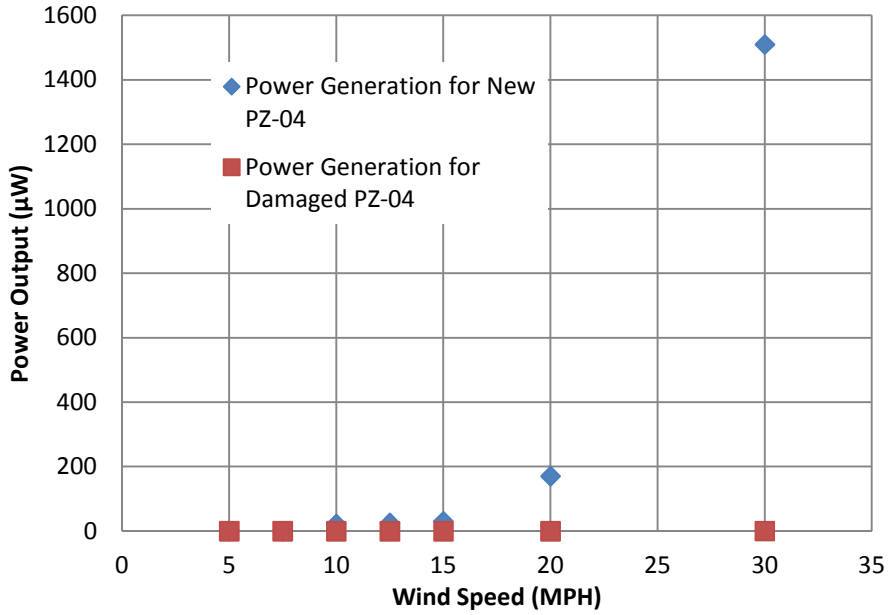

Figure 32. New vs. damaged PZ-04 power output.

7.4 Bluff Body Test Results

In Ch. 4, VIV was introduced followed by bluff body excitations. The testing procedures followed the same progressive development of methods, and bluff body excitations were tested along with the results from the previous section. It is important to note that the flag stand used in all tests acts as a bluff body and influences all tests. Given that this is an experimental control of sorts the main focus is given to the additional bluff bodies tested but the flag stand variables are also presented in this Section.

Five separate bluff body shapes were tested and are shown below in Figure 33. From left to right these shapes are referenced as a full cylinder, half cylinder, triangle, large square, and small square.

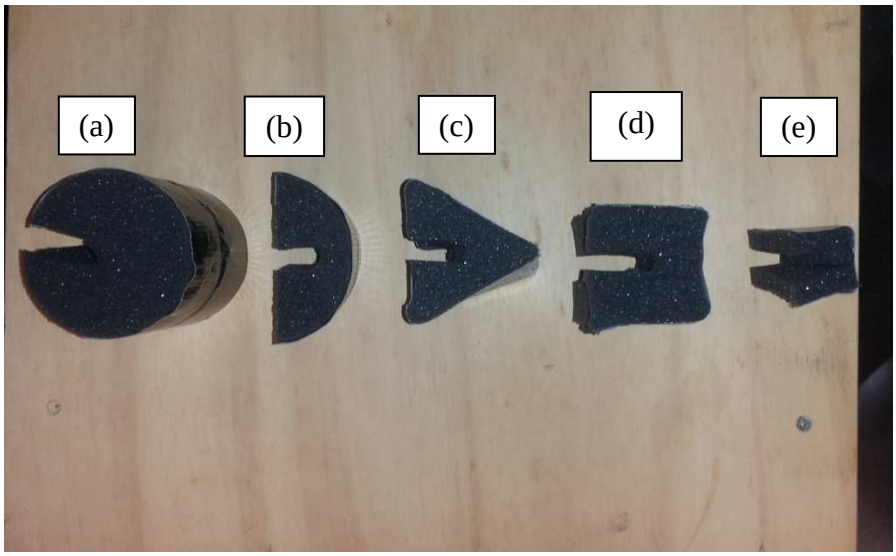

Figure 33. Bluff body shapes tested: (a) full cylinder, (b) half cylinder, (c) triangle, (d) large square, (e) small square.

The material used to manufacture these shapes was foam sourced from McMaster Carr. Due to relatively high porosity of the foam, each piece was layered with duct tape to seal it and produce better results. Equation (11) describes the formula for vortex shedding frequency and was used to calculate the vortex shedding frequencies for each bluff body shape. Due to the varied shapes used in this test the characteristic length, L, from Equation (11) becomes the hydraulic diameter, or D_h, in order to properly calculate f_s. The equation for hydraulic diameter is [127]

$$D_h = \frac{4A}{P} \tag{49}$$

where A is the cross-sectional area, and P is the wetted perimeter. The wetted perimeter is the perimeter of the cross section that experiences fluid flow interaction. Table 2 shows the dimensions of each bluff body along with the calculated hydraulic diameter.

Table 2. Characteristic dimensions for bluff body shapes.

Bluff Body Shape	Flag Stand	Full Cylinder	Half Cylinder	Triangle	Large Square	Small Square
Length x Width or Diameter (in.)	0.5 x 1	3	3	2.5 x 2.25	2 x 2	1 x 1
$D_h(in.)$	0.8	3	3	2.25	2.67	1.33

The flow speeds used in the calculations are the same ones presented in section 7.3. These flow speeds were used to calculate the Reynolds number and subsequently the Strouhal number. For Reynolds numbers ranging from 10^5 to 10^6 a Strouhal number of 0.2 can be used. With this information vortex shedding frequency (f_s) can be calculated for each shape at each flow speed.

Figure 34 shows the vortex shedding frequency versus wind velocity for each bluff body shape tested. Please note that the full and half cylinders have the same vortex shedding frequencies and are therefore overlaid on the graph. As it is shown vortex shedding frequency increases as wind velocity increases with the flag stand having the highest frequencies produced throughout the testing range.

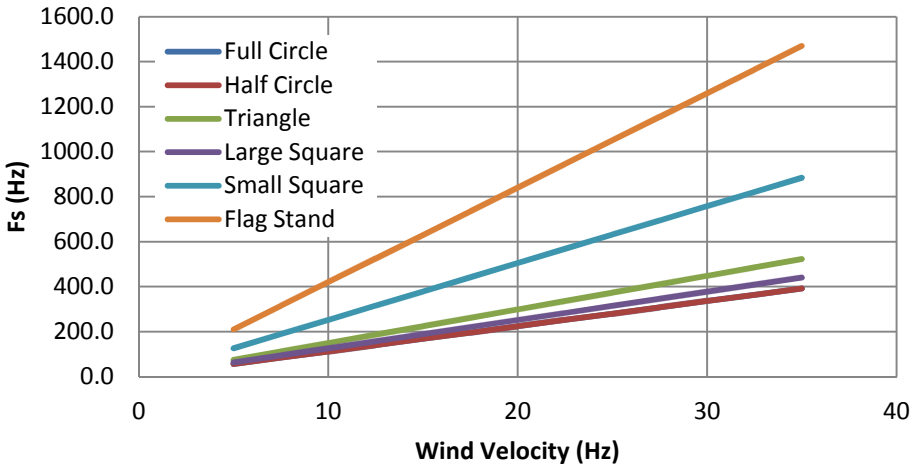

Figure 34. Vortex shedding frequency (Fs) vs. wind velocity for each bluff body shape tested.

Each piezoelectric material was tested with each bluff body in increments of 2.5-5 mph wind velocity. Voltage data was recorded and RMS power calculated in the same manner as section 7.3. Operating frequency was not measured or calculated during these tests. In many cases the measurements were erratic, yielding undesirable results. Displacement measurement through optical means such as a laser vibrometer will be employed in future tests to mitigate this problem. Because the vortex shedding frequency acts as a forcing function on the system one might conclude that the operating frequency for each velocity matches that of the shedding frequency. This is incorrect, however, due to wake production and flow separation by the bluff body. At some velocities the wake produced by the bluff body encloses the entire piezoelectric material, causing system excitation and, therefore, frequency to reduce to nearly zero. Figure 35 shows the PZ-04 PVDF trapped inside the wake of the bluff body. This typically only occurs at the higher end of the tested velocity spectrum.

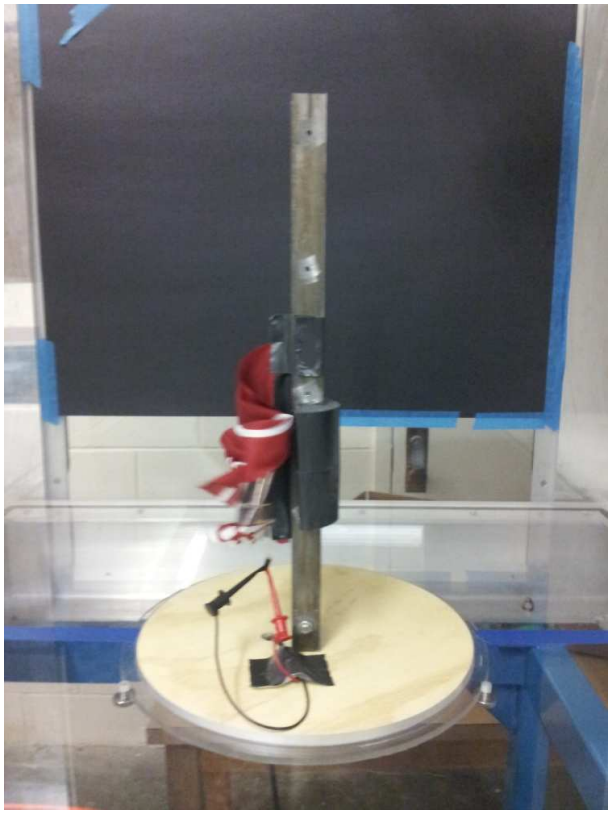

Figure 35. PZ-04 w/ flag body trapped within wake of half cylinder bluff body at 20 mph.

It is also worth noting that wake separation accounts for differences between the performance of the full and half cylinder bluff bodies. While Table 2 shows that their vortex shedding frequencies are indeed the same, the slight variation in bluff body shape does in fact produce different wake characteristics. This has been illustrated in many studies and accounts for the slight power production differences between the two shapes [128-130]. Figures 36 through 41 show the bluff body power production versus wind velocity for each bluff body shape followed by Table 3 which highlights the max power without bluff body, max power with bluff body, and wind velocity at which this power occurs for each material tested. Figures 36 through 41 clearly illustrate that the addition of the bluff bodies to the various materials was generally only useful at higher velocities. Even so, for the majority of the tested velocity ranges the bluff bodies did not increase performance. This suggests that the addition of bluff bodies with these materials would

perhaps be best suited to steady state operating conditions where the vortex shedding frequency can be tuned to the desirable system parameters. Table 3 does illustrate however that for the PZ-02 PVDF, M8557-P2 MFC, and M2814-P2 MFC energy harvesters max power production was significantly increased.

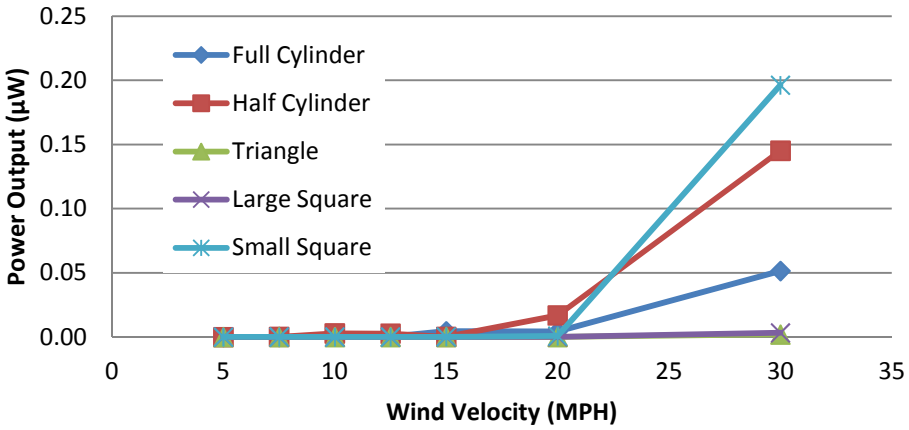

Figure 36. Bluff body power output vs. wind velocity for PZ-04 PVDF.

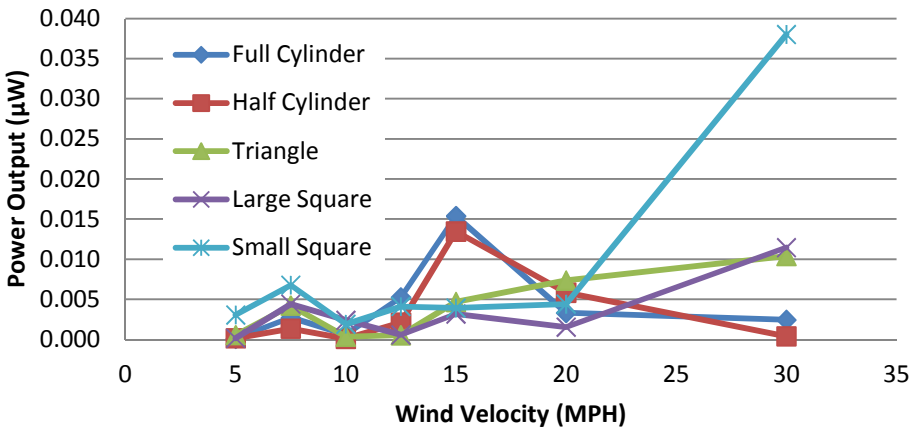

Figure 37. Bluff body power output vs. wind velocity for PZ-04 PVDF with flag body.

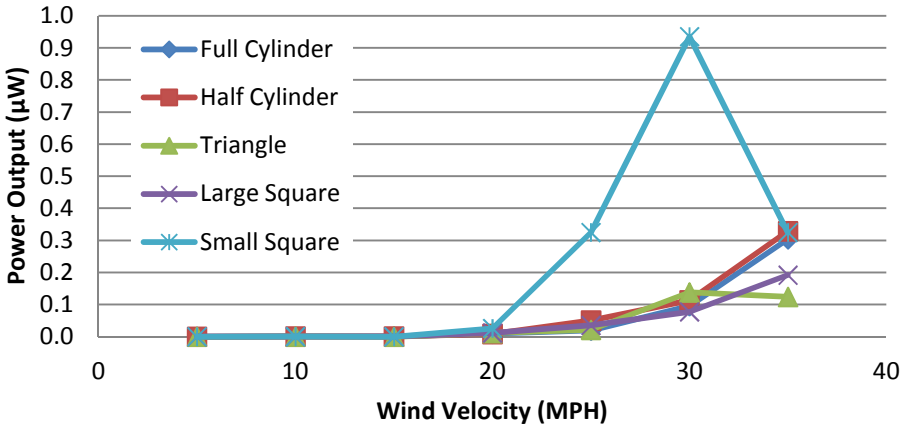

Figure 38. Bluff body power output vs. wind velocity for PZ-02 PVDF.

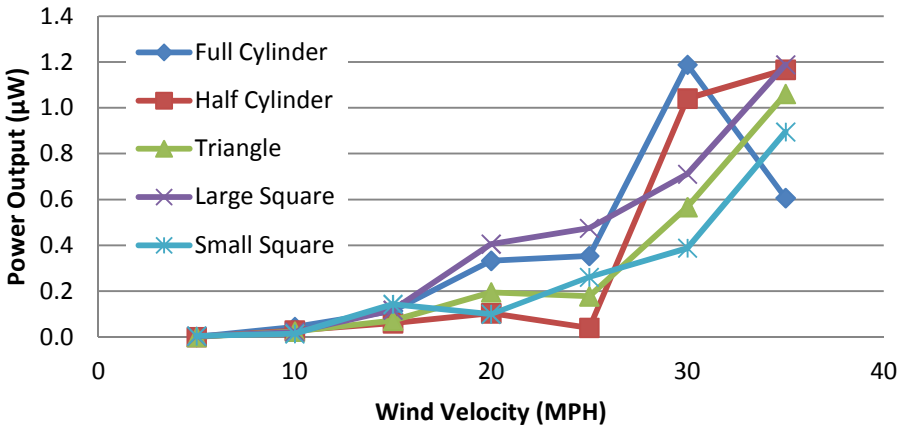

Figure 39. Bluff body power output vs. wind velocity for PZ-02 PVDF with tail section.

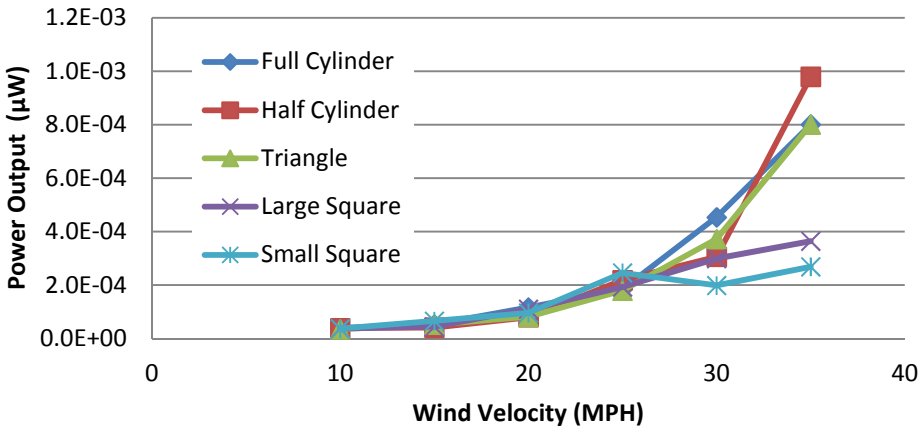

Figure 40. Bluff body power output vs. wind velocity for M8557-P2 MFC.

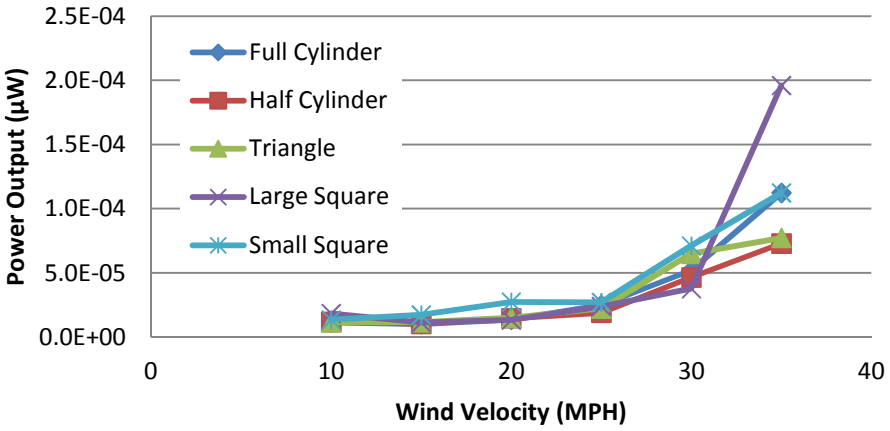

Figure 41. Bluff body power output vs. wind velocity for M2814-P2 MFC.

Table 3. Max power production per material with and without bluff body.

Materials	Max Power w/o Bluff Body (µW)	Wind Velocity (mph)	Max Power w/ Bluff Body (µW)	Wind Velocity (mph)	Bluff Body Shape with Max Power
PZ-04	1.510E+03	30	1.962E-01	30	Small Square
PZ-04 w/ flag body	5.262E+00	30	3.803E-02	30	Small Square
PZ-02	2.663E-01	20	9.351E-01	30	Small Square
PZ-02 w/ tail section	1.884E-01	35	1.188E+00	30	Full Cylinder
M8557-P2	1.904E-04	30	9.797E-04	35	Half Cylinder
M2814-P2	5.329E-05	35	1.960E-04	35	Large Square

CHAPTER 8

DISCUSSION

When it comes to energy production, cost is often the most important factor. Table 4 shows the cost of each material tested in this study as well as its calculated energy production cost. As with overall power production, shown in the previous chapter, the energy production costs between PVDFs and MFCs differ by orders of magnitude. Not only is the overall power output of the MFC extremely low for this study but the cost of production is prohibitive.

Table 4. Piezoelectric material cost and energy production cost.

Material	PZ-04	PZ-02	M8557-P2	M2812-P2
Cost ($)	42.50	6.750	280.00	67.00
Energy Production Cost ($/μW)	0.03	5.68	286000	342000

To further understand the various methods of fluid based energy harvesting it is worth weighing them against one another to better gauge potential advantages currently gained and perhaps yet to be gained. Table 5 lists works previously mentioned in this study and compares their methods, piezoelectric generator types, energy output, and energy density with the results from this study. The energy density is particularly important as it allows a truer measure of one study and method versus another. This is due to the simple fact of experimental differences, differences in phenomenon used, and of course different piezoelectric coefficients of the piezoelectric materials themselves. It is also worth noting that it is not entirely correct to assume

that the method and subsequent experiment with the highest power output is necessarily the best. The end use of the technology will dictate what balance of efficiency, cost, and manufacturability needs to be considered.

Table 5. Fluid based piezoelectric energy harvesting output comparison

Fluid Phenomenon	Application	Piezoelectric Element	Maximum Output (µW)	Energy Density (µW/cm^3)	Reference Number
VIV	Harmonica Chamber	PZT	800	30285	86
VIV	Wind Tunnel	PZT	7	97	91
VIV	Wind Tunnel	PVDF	94	158	91
VIV	Circular Cylinder	PZT	1000	88	92
VIV with Bluff Body	Cylindrical Bluff Body	PVDF	4	298	94
Fluttering	Pinned Airfoil	PZT	2200	452	87
Galloping	Novel Galloping Structure	PZT	53000	18935	105
VIV	Tested PZ-04	PVDF	1510	2179	Current Study
VIV	Tested PZ-04 w/ Flag Body	PVDF	5.3	8	Current Study
VIV with Bluff Body	Tested PZ-02 PVDF w/ Bluff Body	PVDF	0.9	7	Current Study
VIV with Bluff Body	Tested PZ-02 PVDF w/ Tail Section and Bluff Body	PVDF	1.2	9	Current Study
VIV with Bluff Body	Tested M8557-P2 MFC w/ Bluff Body	MFC	9.79E-04	0.5E-03	Current Study
VIV with Bluff Body	Tested M2814-P2 MFC w/ Bluff Body	MFC	1.96E-04	0.9E-03	Current Study

Several things can immediately be seen when looking at Table 5: First, it appears that there does not seem to be a clear distinction between the use of PVDF and PZT piezoelectric energy harvesters in previous studies. This depends highly on the application and in many cases PVDFs are used in fluid excitation due to their increased flexibility over PZTs. PZT's do gain an edge over PVDF's though in that they often have higher piezoelectric coefficients. This is examined in detail with the direct comparison of both PVDF and PZT harvesters in both wind and water tests [91]. Despite inferior piezoelectric constants, in both cases, the PVDF produced a superior output to the PZT. Another observation one could make about the table is that the flutter and galloping based methods produce higher outputs than many of the vortex induced methods. While this is true is does come at a cost. That cost ties power output and power density together. The power density is the power output per unit volume. The power densities achieved from galloping and fluttering are superior to other methods except for the harmonica chamber example and the PZ-04 tested in this study [86]. This gain can be offset by the narrow bandwidth that is sometimes characteristic of aeroelastic based systems. This occurs due to the need to operate galloping and fluttering systems at their natural frequencies. While all systems discussed work best at their natural frequencies it is all but a requirement for galloping and fluttering systems in order to achieve any amount of desirable gains. Conversely, mainly vortex based designs will operate within larger bandwidths as discussed previously in the bluff body section. When analyzing the data presented by Tables 3-5 together one can see that this study makes a very strong case for the use of PVDF energy harvesters in wind-based applications of a similar device structure. The PZ-04 PVDF produced more power at a lower unit cost than any other material tested in this study. When the PZ-04 is weighed against previous works it is the highest

performing PVDF wind-based harvester of this study. Further work with PVDFs in these applications is certainly warranted.

These pros and cons between different types of piezoelectric harvesters, fluid phenomenon, and power management options offer researchers and industry many options moving forward. It is quite possible that applications dictating moderate system deflection, wide operating bandwidth, and higher flow speeds will incorporate VIV based designs using PZT's; while other systems requiring higher degrees of motion, narrower operating bandwidth, and lower flow speeds many incorporate flutter or galloping based designs with PVDF. Numerous other combinations exist in between to suit the need.

There remains another key area where large gains can be made with piezoelectric energy harvesters and that is concerning the power generation itself and conversion. Once the energy is converted by the generator it can be stored and managed in a variety of ways. A simple wave rectifier can be used to convert the AC signal to a DC signal that can then be stored in a capacitor or battery as mentioned earlier. Additionally Synchronized Switch Harvesting on Inductor or SSHI methods have been compared against a simple resistive load and a rectifier circuit [131]. It was concluded that the SSHI method offered clear gains over other methods and most notably when system coupling was low. Further development of this approach used velocity control rather than the traditional bipolar transistor to effectively create the V-SSHI approach [132]. The device proposed proved to be fully self powered while offering gains of up to 200%.

The final frontier in energy harvesting may in fact be active energy harvesting. In active energy harvesting we are typically monitoring the system through some means and then actively changing the system dynamics in real time to meet changing environmental dynamics. In this way the energy harvester adapts to the environment, stays within its optimum operating range,

and generates higher outputs for greater periods of time. This is a very new field but there have been several studies released already. One such study uses switch-mode power electronics to control the voltage or charge on the piezoelectric device relative to the mechanical input for optimized energy conversion [133]. This is similar to impedance matching between the system parameters. Power generation was increased by a factor of five compared to traditional rectifier based methods. Another study actually uses a secondary piezoelectric device as a means of system monitoring [134]. In this study a cantilever beam is outfitted with a piezoelectric disk for sensing system deflection and a piezoelectric bimorph for both harvesting and control. One layer is used to alter the stiffness of the system while the other layer is used to harvest energy. A frequency self tuning scheme is employed along with associative electronics to complete the system. Tests revealed maximum power generation of 0.45 mW and a power density of 2.9 mW/cm^3. The bandwidth was also increased by a factor of four. If we were to include this in Table 5 it would measure favorable against the wind-based methods. However, since this was a pure vibration study it was left out of direct comparison. With such substantial gains to be found through active energy harvesting further research should be expected in this area.

8.1 Recommendations for Future Works

The results of this study indicate that a maximum power production of roughly 1.5 mW at 30 mph with an overall energy density of 2179 μW/cm^3 can be achieved with a flag-like PVDF energy harvester excited by wind flow. While the progression of this work could take many forms there seem to be several logical steps to be taken next: Additional analytical and computation analysis is needed to better understand the system dynamics of the base piezoelectric-flag system. The system modeling presented in Ch.5 offers a simplified approach to the complex system with reasonable first term results. The experimental frequencies when

matched against the results from Ch.6 show an error of roughly 20-30%. There are many possible reasons for this including, but not limited to, system damping being neglected, impedance matching of the experimental setup being neglected, or perhaps system nonlinearities being neglected. Once the system dynamics are better understood then perhaps FEA modeling could offer other useful insights.

While the preliminary results for the contributions of bluff bodies on this study seem limited, there were favorable results gained from the PZ-02 PVDF harvester. These bluff body effects were not within the original scope of this study so their addition should be considered an addendum at this point. For greater insights, future work will be done to calculate the natural frequency of each harvester and match it to the vortex shedding frequency of various bluff bodies. This vortex shedding frequency can be visualized through various fluid modeling programs if one wishes to compare the results to other such works.

Additionally, the area of active energy harvesting offers interesting possibilities. To this author's knowledge no studies have been conducted on active energy harvesting of a fluid based vibration. This could logically be achieved through the use of existing power conditioning methods, or perhaps more interestingly, through the manipulation of vortex generation. Active bluff bodies could tune the vortex shedding frequencies to various wind velocities thereby increasing operating bandwidth and potentially power output as well.

CHAPTER 9

CONCLUSION

It should be clear by now that piezoelectric energy harvesters offer advanced opportunities to power generation problems. Since piezoelectric devices require direct strain to generate power the piezoelectric coefficients themselves will have to improve over time if greater gains are to be realized. However, since this is roughly all that is required to generate power there are clear advantages over other means of energy harvesting, such as electromagnetic or thermoelectric, due to their relative complex geometries and mechanisms.

A brief history into the purpose and potential applications of energy harvesters has been given. Various types of energy harvesting techniques were discussed in which piezoelectric energy harvesting was chosen as the focal point. Early examples of harvesting techniques were discussed following an introduction into the basics of the piezoelectric principle and its important aspects. Basic dynamics of a piezoelectric system including system nonlinearities were also mentioned. Wind-based energy harvesting was then presented as a sub-field of piezoelectric energy harvesting and supported by various fluid based phenomenon. PVDFs were then introduced allowing the generation of a unique flag based energy harvester design. Modeling techniques, assumptions, and methods were presented along with analytical and experimental results. MFC piezoelectric harvesters were tested alongside the PVDF harvesters. The results were correlated against each other finding that indeed the PVDF is the ideal piezoelectric material for a flag-like energy harvester in a wind flow. Although the MFC harvesters had higher piezoelectric coefficients the more flexible PVDFs harvesters were able to generate more power from a given input. The extreme flexibility of the PVDF harvester allows the entire harvester to

achieve some degree of deflection during excitation. In contrast, the MFC harvesters act more like a traditional cantilever beam with more localized areas of defection.

Finally the future of the field was discussed. It is this author's belief that the developing areas of energy harvesting research will incorporate active control theories and methods in harmony with energy harvesting systems. With continual advancements of the piezoelectric coefficient of materials over time, piezoelectric energy harvesting will further distance itself from other methods of energy harvesting as the dominant form.

REFERENCES

[1] Trager, E. C., 2009, "Volume 4: Ocean Engineering; Ocean Renewable Energy; Ocean Space Utilization, Parts A and B; Where We Are Now: The U.S. Federal Regulatory Framework for Alternative Energy on the OCS " pp. 1169 - 1179.

[2] Holdren, J. P., 2007, "Energy and Sustainability " Science (New York, N.Y.), 315(5813) pp. 737.

[3] Cook-Chennault, K. A., Thambi, N., Bitetto, M. A., 2008, "Piezoelectric Energy Harvesting: A Green and Clean Alternative for Sustained Power Production " Bulletin of Science, Technology & Society, 28(6) pp. 496 - 509.

[4] Enz, C. C., El-Hoiydi, A., Decotignie, J. -., 2004, "WiseNET: An Ultralow-Power Wireless Sensor Network Solution " Computer, 37(8) pp. 62 - 70.

[5] Anton, S. R., and Inman, D. J., 2008, "Vibration energy harvesting for unmanned aerial vehicles," Active and Passive Smart Structures and Integrated Systems 2008, SPIE - The International Society for Optical Engineering, USA, 6928, pp. 692824-1.

[6] Wang, Z. L., 2008; 2008, "Energy Harvesting for Self-Powered Nanosystems " Nano Research, 1(1) pp. 1 - 8.

[7] Ansari, S. A., Żbikowski, R., and Knowles, K., 2006, "Aerodynamic Modelling of Insect-Like Flapping Flight for Microscale Air Vehicles " Progress in Aerospace Sciences, 42(2) pp. 129 - 172.

[8] Aktakka, E. E., Kim, H., and Najafi, K., 2011; 2011, "Energy Scavenging from Insect Flight " Journal of Microscalemechanics and Microscaleengineering, 21(9) pp. 095016.

[9] Palumbo, A., Amato, F., Calabrese, B., 2010, "An embedded system for EEG acquisition and processing for brain computer interface applications," Wearable and Autonomous Biomedical Devices and Systems for Smart Environment - Issues and Characterization, Springer Verlag, Tiergartenstrasse 17, Heidelberg, D-69121, Germany, 75 LNEE, pp. 137-154.

[10] Sodano, H. A., Inman, D. J., and Park, G., 2005, "Comparison of Piezoelectric Energy Harvesting Devices for Recharging Batteries," Journal of Intelligent Material Systems and Structures, 16(10) pp. 799-807.

[11] Roundy, S., Wright, P. K., and Rabaey, J., 2003, "A Study of Low Level Vibrations as a Power Source for Wireless Sensor Nodes " Computer Communications, 26(11) pp. 1131 - 1144.

[12] Ali, S. F., Friswell, M. I., and Adhikari, S., 2011, "Analysis of Energy Harvesters for Highway Bridges," Journal of Intelligent Material Systems and Structures, 22(16) pp. 1929-1938.

[13] Erturk, A., 2011, "Piezoelectric Energy Harvesting for Civil Infrastructure System Applications: Moving Loads and Surface Strain Fluctuations," Journal of Intelligent Material Systems and Structures, 22(17) pp. 1959-1973.

[14] Beeby, S. P., Tudor, M. J., and White, N. M., 2006, "Energy Harvesting Vibration Sources for Microscalesystems Applications," Measurement Science & Technology, 17(12) pp. 175-95.

[15] Zhu, D., Beeby, S., Tudor, J., 2011, "Improving output power of piezoelectric energy harvesters using multilayer structures," 25th Eurosensors Conference, September 4, 2011 - September 7, Elsevier Ltd, Athens, Greece, 25, pp. 199-202.

[16] Roundy, S., Leland, E. S., Baker, J., 2005, "Improving Power Output for Vibration-Based Energy Scavengers," IEEE Pervasive Computing, 4(1) pp. 28-36.

[17] Curie, J., and Curie, P., 1880, "Développement, Par Pression, De l'électricité Polaire Dans Les Cristaux Hémièdres à Faces Inclinées," Comptes Rendus De l'Académie Des Sciences. Série II. Fascicule a, Sciences De La Terre Et Des planètes, 91pp. 294.

[18] Jalili <component_number> Chapter 6, N., 2010; 2009, "Piezoelectric-Based Vibration Control; Physical Principles and Constitutive Models of Piezoelectric Materials " pp. 129 - 159.

[19] Zhu, D., Beeby, S., Tudor, J., 2011, "Improving output power of piezoelectric energy harvesters using multilayer structures," 25th Eurosensors Conference, September 4, 2011 - September 7, Elsevier Ltd, Athens, Greece, 25, pp. 199-202.

[20] Li, L., Wu, J., Chu, X., 2008, "Finite Element Analysis and Experiment on Piezoelectric Bimorph," Guangxue Jingmi Gongcheng/Optics and Precision Engineering, 16(12) pp. 2378-2383.

[21] Sodano, H. A., Inman, D. J., and Park, G., 2004, "A Review of Power Harvesting from Vibration using Piezoelectric Materials," Shock and Vibration Digest, 36(3) pp. 197-205.

[22] Dr. Sui Wing, 2003, "Overview of Smart Materials Technology," 2011(04/16) .

[23] Goldarb, M., and Jones, L. D., 1999, "On the Efficiency of Electric Power Generation with Piezoelectric Ceramic," Transactions of the ASME.Journal of Dynamic Systems, Measurement and Control, 121(3) pp. 566-71.

[24] Umeda, M., Nakamura, K., and Ueha, S., 1996, "Analysis of the transformation of mechanical impact energy to electric energy using piezoelectric vibrator," 16th Symposium on Ultrasonic Electronics (USE95), Publication Office, Japanese Journal Appl. Phys, Japan, 35, pp. 3267-73.

[25] Umeda, M., Nakamura, K., and Ueha, S., 1997, "Energy Storage Characteristics of a Piezo-Generator using Impact Induced Vibration," Japanese Journal of Applied Physics, Part 1: Regular Papers & Short Notes & Review Papers, 36(5) pp. 3146-3151.

[26] Sodano, H. A., 2005, "Comparison of Piezoelectric Energy Harvesting Devices for Recharging Batteries " Journal of Intelligent Material Systems and Structures, 16(10) pp. 799 - 807.

[27] Roundy, S., and Wright, P. K., 2004, "A Piezoelectric Vibration Based Generator for Wireless Electronics," Smart Materials and Structures, 13(5) pp. 1131-1142.

[28] Cho, J., Anderson, M., Richards, R., 2005, "Optimization of Electromechanical Coupling for a Thin-Film PZT Membrane: I. Modeling," Journal of Microscalemechanics and Microscaleengineering, 15(10) pp. 1797-803.

[29] Stephen, N. G., 2006, "On Energy Harvesting from Ambient Vibration," Journal of Sound and Vibration, 293(1-2) pp. 409-25.

[30] Liao, Y., and Sodano, H. A., 2008, "Model of a Single Mode Energy Harvester and Properties for Optimal Power Generation," Smart Materials and Structures, 17(6) pp. 065026 (14 pp.).

[31] Challa, V. R., Prasad, M. G., Shi, Y., 2008, "A Vibration Energy Harvesting Device with Bidirectional Resonance Frequency Tunability," Smart Materials and Structures, 17(1) pp. 015035 (10 pp.).

[32] Renno, J. M., Daqaq, M. F., and Inman, D. J., 2009, "On the Optimal Energy Harvesting from a Vibration Source," Journal of Sound and Vibration, 320(1-2) pp. 386-405.

[33] du Toit, N. E., and Wardle, B. L., 2007, "Experimental Verification of Models for Microscalefabricated Piezoelectric Vibration Energy Harvesters," AIAA Journal, 45(5) pp. 1126-37.

[34] McInnes, C. R., Gorman, D. G., and Cartmell, M. P., 2008, "Enhanced Vibrational Energy Harvesting using Nonlinear Stochastic Resonance," Journal of Sound and Vibration, 318(4-5) pp. 655-662.

[35] Cottone, F., Vocca, H., and Gammaitoni, L., 2009, "Nonlinear Energy Harvesting," Physical Review Letters, 102(8) pp. 080601 (4 pp.).

[36] Mann, B. P., and Sims, N. D., 2009, "Energy Harvesting from the Nonlinear Oscillations of Magnetic Levitation," Journal of Sound and Vibration, 319(1-2) pp. 515-530.

[37] Kim, H., Tadesse, Y., and Priya, S., 2009, "Energy Harvesting Technologies,"Springer US, pp. 3-39.

[38] Farnell, D. J. J., David, T., and Barton, D. C., 2004, "Coupled States of Flapping Flags," Journal of Fluids and Structures, 19(1) pp. 29-36.

[39] Mahmoodi, S. N., Daqaq, M. F., and Jalili, N., 2009, "On the Nonlinear-Flexural Response of Piezoelectrically Driven Microscalecantilever Sensors," Sensors and Actuators A: Physical, 153(2) pp. 171-179.

[40] Mahmoodi, S. N., and Jalili, N., 2007, "Non-Linear Vibrations and Frequency Response Analysis of Piezoelectrically Driven Microscalecantilevers," International Journal of Non-Linear Mechanics, 42(4) pp. 577-587.

[41] Braun, S., 2002, "Encyclopedia of vibration," Academic Press, San Diego, .

[42] Ou, Q., Chen, X., Gutschmidt, S., 2012; 2012, "An Experimentally Validated Double-Mass Piezoelectric Cantilever Model for Broadband Vibration-Based Energy Harvesting " Journal of Intelligent Material Systems and Structures, 23(2) pp. 117 - 126.

[43] Delnavaz, A.,Mahmoodi, S. N., Jalili, N., 2010, "Linear and Non-Linear Vibration and Frequency Response Analyses of Microscalecantilevers Subjected to Tip-Sample Interaction," International Journal of Non-Linear Mechanics, 45(2) pp. 176-85.

[44] Mahmoodi, S. N., Jalili, N., and Khadem, S. E., 2008, "An Experimental Investigation of Nonlinear Vibration and Frequency Response Analysis of Cantilever Viscoelastic Beams " Journal of Sound and Vibration, 311(3-5) pp. 1409 - 1419.

[45] Mahmoodi, S. N., Craft, M. J., Southward, S. C., 2011, "Active Vibration Control using Optimized Modified Acceleration Feedback with Adaptive Line Enhancer for Frequency Tracking," Journal of Sound and Vibration, 330(7) pp. 1300-1311.

[46] Stanton, S. C., McGehee, C. C., and Mann, B. P., 2010, "Nonlinear Dynamics for Broadband Energy Harvesting: Investigation of a Bistable Piezoelectric Inertial Generator," Physica D: Nonlinear Phenomena, 239(10) pp. 640-653.

[47] Stanton, S. C., Mann, B. P., and Owens, B. A. M., 2012, "Melnikov Theoretic Methods for Characterizing the Dynamics of the Bistable Piezoelectric Inertial Generator in Complex Spectral Environments," Physica D: Nonlinear Phenomena, 241(6) pp. 711-720.

[48] Owens, B. A. M., and Mann, B. P., 2012, "Linear and Nonlinear Electromagnetic Coupling Models in Vibration-Based Energy Harvesting," Journal of Sound and Vibration, 331(4) pp. 922-937.

[49] Abdelkefi, A., Nayfeh, A. H., Hajj, M. R., 2012; 2012, "Energy Harvesting from a Multifrequency Response of a Tuned bending–torsion System " Smart Materials and Structures, 21(7) pp. 075029.

[50] Abdelkefi, A., Nayfeh, A. H., and Hajj, M. R., 2012, "Modeling and Analysis of Piezoaeroelastic Energy Harvesters," Nonlinear Dynamics, 67(2) pp. 925-939.

[51] Daqaq, M. F., 2012, "On Intentional Introduction of Stiffness Nonlinearities for Energy Harvesting Under White Gaussian Excitations," Nonlinear Dynamics, 69(3) pp. 1063-1079.

[52] Mahmoodi, S. N., Jalili, N., 2008, "Coupled Flexural-Torsional Nonlinear Vibrations of Piezoelectrically Actuated Microscalecantilevers with Application to Friction Force Microscalescopy," Journal of Vibration and Acoustics, Transactions of the ASME, 130(6) .

[53] Preumont, A., "Vibration control of active structures: an introduction " Dordrecht ; Kluwer Academic Publishers, c1997., pp. 259.

[54] Mahmoodi, S. N., Jalili, N., 2009, "Piezoelectrically Actuated Microscalecantilevers: An Experimental Nonlinear Vibration Analysis," Sensors and Actuators A: Physical, 150(1) pp. 131-136.

[55] Mahmoodi, S. N., Jalili, N., and Ahmadian, M., 2009; 2010, "Subharmonics Analysis of Nonlinear Flexural Vibrations of Piezoelectrically Actuated Microscalecantilevers " Nonlinear Dynamics, 59(3) pp. 397 - 409.

[56] Jia, D., and Liu, J., 2009, "Human Power-Based Energy Harvesting Strategies for Mobile Electronic Devices," Frontiers of Energy and Power Engineering in China, 3(1) pp. 27-46.

[57] Starner, T., 1996, "Human-Powered Wearable Computing " IBM Systems Journal, 35(3.4) pp. 618 - 629.

[58] Gonzalez, J. L., Rubio, A., and Moll, F., 2001, "A prospect on the use of piezoelectric effect to supply power to wearable electronic devices," Proceedings of the Fourth International Conference on Materials Engineering for Resources, Akita Univ, Akita, Japan, 1, pp. 202-7.

[59] Antaki, J. F., Bertocci, G. E., Green, E. C., 1995, "A gait-powered autologous battery charging system for artificial organs," J.B. Lippincott Co, Hagerstown, MD, United States, 41, pp. M588-M595.

[60] Wei, X., and Liu, J., 2008, "Power Sources and Electrical Recharging Strategies for Implantable Medical Devices," Frontiers of Energy and Power Engineering in China, 2(1) pp. 1-13.

[61] Ando, B., Baglio, S., Ferrari, M., 2010, "Nonlinear dynamics, materials and integrated devices for energy harvesting in wearable sensors," Wearable and Autonomous Biomedical Devices and Systems for Smart Environment - Issues and Characterization, Springer Verlag, Tiergartenstrasse 17, Heidelberg, D-69121, Germany, 75 LNEE, pp. 97-113.

[62] Borges, L. M., Araujo, P., Lebres, A. S., 2010, "Wearable sensors for foetal movement monitoring in low risk pregnancies," Wearable and Autonomous Biomedical Devices and Systems for Smart Environment - Issues and Characterization, Springer Verlag, Tiergartenstrasse 17, Heidelberg, D-69121, Germany, 75 LNEE, pp. 115-136.

[63] Francesco, C., Antonio, G., and Sergio, C., 2010, "Smart nano-systems for tumour cellular diagnoses and therapies," Wearable and Autonomous Biomedical Devices and Systems for Smart Environment - Issues and Characterization, Springer Verlag, Tiergartenstrasse 17, Heidelberg, D-69121, Germany, 75 LNEE, pp. 31-54.

[64] Ven, V. D., Bourke, A., Nelson, J., 2010, "Design and integration of fall and mobility monitors in health monitoring platforms," Wearable and Autonomous Biomedical Devices and Systems for Smart Environment - Issues and Characterization, Springer Verlag, Tiergartenstrasse 17, Heidelberg, D-69121, Germany, 75 LNEE, pp. 1-29.

[65] Borges, L. M., Barroca, N., Velez, F. J., 2009, "Smart-clothing wireless flex sensor belt network for foetal health monitoring," 3rd International Conference on Pervasive Computing Technologies for Healthcare (Pervasive Health 2009), IEEE, Piscataway, NJ, USA, pp. 4.

[66] Platt, S. R., Farritor, S., Garvin, K., 2005, "The use of Piezoelectric Ceramics for Electric Power Generation within Orthopedic Implants," IEEE/ASME Transactions on Mechatronics, 10(4) pp. 455-61.

[67] Lewandowski, B. E., Kilgore, K. L., and Gustafson, K. J., 2009, "In Vivo Demonstration of a Self-Sustaining, Implantable, Stimulated-Muscle-Powered Piezoelectric Generator Prototype," Annals of Biomedical Engineering, 37(11) pp. 2390-2401.

[68] Lewandowski, B. E., Kilgore, K. L., and Gustafson, K. J., 2007, "Design Considerations for an Implantable, Muscle Powered Piezoelectric System for Generating Electrical Power," Annals of Biomedical Engineering, 35(4) pp. 631-41.

[69] Ramsay, M. J., and Clark, W. W., 2001, "Piezoelectric energy harvesting for bio MEMS applications," Smart Structures and Materials 2001: Industrial and Commercial Applications of Smart Structures Technologies, SPIE-Int. Soc. Opt. Eng, USA, 4332, pp. 429-38.

[70] Sohn, J. W., Chor, S. B., and Lee, D. Y., 2005, "An Investigation on Piezoelectric Energy Harvesting for MEMS Power Sources," Proceedings of the Institution of Mechanical Engineers, Part C (Journal of Mechanical Engineering Science), 219pp. 429-36.

[71] Amin Karami, M., and Inman, D. J., 2012, "Powering Pacemakers from Heartbeat Vibrations using Linear and Nonlinear Energy Harvesters " Applied Physics Letters, 100(4) pp. 042901.

[72] Daoutis, L. G., and Dialynas, E. N., 2009, "Impact of Hybrid Wind and Hydroelectric Power Generation on the Operational Performance of Isolated Power Systems," Electric Power Systems Research, 79(10) pp. 1360-1373.

[73] Glasnovic, Z., and Margeta, J., 2009, "The Features of Sustainable Solar Hydroelectric Power Plant," Renewable Energy, 34(7) pp. 1742-1751.

[74] Wikipedia, 2012, "Wind Turbine," 2012.

[75] Kaldellis, J.K., and Zafirakis, D.P., 2012, "Comprehensive Renewable Energy,"Elsevier, Oxford, pp. 671-724.

[76] Porté-Agel, F., Wu, Y., Lu, H., 2011, "Large-Eddy Simulation of Atmospheric Boundary Layer Flow through Wind Turbines and Wind Farms," Journal of Wind Engineering and Industrial Aerodynamics, 99(4) pp. 154-168.

[77] Saranyasoontorn, K., and Manuel, L., 2004, "Efficient Models for Wind Turbine Extreme Loads using Inverse Reliability," Journal of Wind Engineering and Industrial Aerodynamics, 92(10) pp. 789-804.

[78] Rosen, A., and Sheinman, Y., 1994, "The Average Output Power of a Wind Turbine in a Turbulent Wind," Journal of Wind Engineering and Industrial Aerodynamics, 51(3) pp. 287-302.

[79] Mitcheson, P. D., Yeatman, E. M., Rao, G. K., 2008, "Energy Harvesting from Human and Machine Motion for Wireless Electronic Devices," Proceedings of the IEEE, 96(9) pp. 1457-86.

[80] W.J. Duncan., 1945, "The Fundamentals of Flutter " Aircraft Engineering and Aerospace Technology, 17(2; 17) pp. 32-38.

[81] Hyung-Jo Jung, and Seung-Woo Lee, 2011, "The Experimental Validation of a New Energy Harvesting System Based on the Wake Galloping Phenomenon," Smart Materials and Structures, 20(5) pp. 055022 (10 pp.).

[82] Sarpkaya, T., 2004, "A Critical Review of the Intrinsic Nature of Vortex-Induced Vibrations," Journal of Fluids and Structures, 19(4) pp. 389-447.

[83] Bearman, P. W., 2009, "Understanding and Predicting Vortex-Induced Vibrations," Journal of Fluid Mechanics, 634pp. 1-4.

[84] Williamson, C. H. K., and Govardhan, R., 2008, "A Brief Review of Recent Results in Vortex-Induced Vibrations," Journal of Wind Engineering and Industrial Aerodynamics, 96(6-7) pp. 713-35.

[85] Williamson, C.H.K., and Govardhan, R., 2004, Annual Reviews, Palo Alto, CA, USA, pp. 413-55.

[86] Bibo, A., Li, G., and Daqaq, M. F., 2011, "Electromechanical Modeling and Normal Form Analysis of an Aeroelastic Microscale-Power Generator," Journal of Intelligent Material Systems and Structures, 22(6) pp. 577-592.

[87] Bryant, M., and Garcia, E., 2011, "Modeling and Testing of a Novel Aeroelastic Flutter Energy Harvester," Journal of Vibration and Acoustics, Transactions of the ASME, 133(1) .

[88] Wang, D. , and Chang, K. , 2010, "Electromagnetic Energy Harvesting from Flow Induced Vibration," Microscaleelectronics Journal, 41(6) pp. 356-64.

[89] Sheets, C., and French, J., 2012, "Effect of Geometric And Material Variation of Flow-Induced Microscale Energy Harvester For Localized Wind Environment," Proceedings of the ASME 2012 Conference on Smart Materials, Adaptive Structures and Intelligent Systems, .

[90] De, M.,Jr, Vieira, W. G. R., Erturk, A., 2011, "Modeling and Analysis of Piezoelectric Energy Harvesting from Aeroelastic Vibrations using the Doublet-Lattice Method," Journal of Vibration and Acoustics, Transactions of the ASME, 133(1) .

[91] Vatansever, D., Hadimani, R. L., Shah, T., 2011, "An Investigation of Energy Harvesting from Renewable Sources with PVDF and PZT," Smart Materials and Structures, 20(5) pp. 055019 (6 pp.).

[92] Xie, J., Yang, J., Hu, H., 2011; 2012, "A Piezoelectric Energy Harvester Based on Flow-Induced Flexural Vibration of a Circular Cylinder " Journal of Intelligent Material Systems and Structures, 23(2) pp. 135 - 139.

[93] Sivadas, V., and Wickenheiser, A. M., 2011, "A study of several vortex-induced vibration techniques for piezoelectric wind energy harvesting," Active and Passive Smart Structures and Integrated Systems 2011, SPIE - The International Society for Optical Engineering, USA, 7977, pp. 79770F (13 pp.).

[94] AkaydIn, H. D., Elvin, N., and Andreopoulos, Y., 2010, "Wake of a Cylinder: A Paradigm for Energy Harvesting with Piezoelectric Materials," Experiments in Fluids, 49(1) pp. 291-304.

[95] Shukla, S., Govardhan, R. N., and Arakeri, J. H., 2009, "Flow Over a Cylinder with a Hinged-Splitter Plate," Journal of Fluids and Structures, 25(4) pp. 713-720.

[96] Taylor, G. W., Burns, J. R., Kammann, S. A., 2001, "The Energy Harvesting Eel: A Small Subsurface ocean/river Power Generator," IEEE Journal of Oceanic Engineering, 26(4) pp. 539-47.

[97] Nakamura, Y., and Yoshimura, T., 1982, "Flutter and Vortex Excitation of Rectangular Prisms in Pure Torsion in Smooth and Turbulent Flows," Journal of Sound and Vibration, 84(3) pp. 305-17.

[98] Tang, L., Paidoussis, M. P., and Jiang, J., 2009, "Cantilevered Flexible Plates in Axial Flow: Energy Transfer and the Concept of Flutter-Mill," Journal of Sound and Vibration, 326(1-2) pp. 263-276.

[99] Elvin, N. G., and Elvin, A. A., 2009, "The Flutter Response of a Piezoelectrically Damped Cantilever Pipe," Journal of Intelligent Material Systems and Structures, 20(16) pp. 2017-2026.

[100] Herbert, C., Cowan, D., Attar, P., 2012, "Aerodynamic Flutter Banner," AIAA: Exploring Stuctural Dynamics, .

[101] Erturk, A., Vieira, W. G. R., De Marqui, C., 2010, "On the Energy Harvesting Potential of Piezoaeroelastic Systems " Applied Physics Letters, 96(18) pp. 184103.

[102] Bibo, A., and Daqaq, M., 2012, " Energy Harvesting Under Combined Aerodynamic And Base Excitation," Proceedings of the ASME 2012 Conference on Smart Materials, Adaptive Structures and Intelligent Systems.

[103] Bryant, M., Garcia, E., and Tse, R., 2012, "
Investigation of Host Stucture Compliance in Aeroelastic Energy Harvesting ," Proceedings of the ASME 2012 Conference on Smart Materials, Adaptive Structures and Intelligent Systems.

[104] Chabart, O., and Lilien, J. L., 1998, "Galloping of Electrical Lines in Wind Tunnel Facilities," Journal of Wind Engineering and Industrial Aerodynamics, 74-76pp. 967-976.

[105] Sirohi, J., and Mahadik, R., 2011, "Piezoelectric Wind Energy Harvester for Low-Power Sensors," Journal of Intelligent Material Systems and Structures, 22(18) pp. 2215-2228.

[106] Liya, Z., Lihua, T., and Yoawen, Y., 2012, “Small Wind Energy Harvesting From Galloping Using Piezoelectric Materials," Proceedings of the ASME 2012 Conference on Smart Materials, Adaptive Structures and Intelligent Systems.

[107] Howell, R. M., Lucey, A. D., Carpenter, P. W., 2009, "Interaction between a Cantilevered-Free Flexible Plate and Ideal Flow," Journal of Fluids and Structures, 25(3) pp. 544-566.

[108] Moretti, P. M., 2004, "Flag Flutter Amplitudes," Flow Induced Vibrations, de Langre & Axisa ed., Ecole Polytechnique, Paris, I, pp. 113-118.

[109] Doaré, O., and Michelin, S., 2011, "Piezoelectric Coupling in Energy-Harvesting Fluttering Flexible Plates: Linear Stability Analysis and Conversion Efficiency," Journal of Fluids and Structures, 27(8) pp. 1357-1375.

[110] Connell, B. S. H., and Yue, D. K. P., 2007, "Flapping Dynamics of a Flag in a Uniform Stream," Journal of Fluid Mechanics, 581pp. 33-67.

[111] Moretti, P. M., 2002, "Flutter in Webs," Flutter in Webs, T.U. Darmstadt, Kaiserslautern, Germany, .

[112] Michelin, S., Smith, S. G. L., and Glover, B. J., 2008, "Vortex Shedding Model of a Flapping Flag," Journal of Fluid Mechanics, 617pp. 1-10.

[113] Martin, A., 2003, "Experimental Study of Drag from a Fluttering Flag," .

[114] Moretti, P. M., 2003, "Tension in fluttering flags," Proceedings of the Tenth International Congress on Sound and Vibration, July 7, 2003 - July 10, Institute of Acoustics, Stockholm, Sweden, pp. 2123-2130.

[115] Images SI Inc., "Piezo Film Sensors Technical Manual," 2012.

[116] Preumont, A., 2006, "Mechatronics: Dynamics of Electromechanical and Piezoelectric Systems,"Springer Netherlands, pp. 95-130.

[117] Preumont, A., 2006, "Mechatronics: Dynamics of Electromechanical and Piezoelectric Systems,"Springer Netherlands, pp. 131-157.

[118] Tanaka, H., 1994, "Generalized Basic Equations for Bending Motions of Piezoelectric Bars Formulated from Hamilton's Principle," Journal of the Acoustical Society of America, 95(4) pp. 1768-72.

[119] Tiersten, H. F., 1967, "Hamilton's Principle for Linear Piezoelectric Media," Proceedings of the Institution of Electrical Engineers, 55(8) pp. 1523-1524.

[120] Watanabe, Y., Isogai, K., Suzuki, S., 2002, "A Theoretical Study of Paper Flutter," Journal of Fluids and Structures, 16(4) pp. 543-560.

[121] Yadykin, Y., Tenetov, V., and Levin, D., 2001, "The Flow Induced Vibration of A Flexible Strip Hanging Vertically In A Parallel Flow; Part 1: Temporal Aeroelastic Instability," Journal of Fluids and Structures, 15(8) pp. 1167-1185.

[122] Yamaguchi, N., Sekiguchi, T., Yokota, K., 2000, "Flutter Limits and Behavior of a Flexible Thin Sheet in High-Speed Flow--- II: Experimental Results and Predicted Behaviors for Low Mass Ratios," Journal of Fluids Engineering, 122(1) pp. 74-83.

[123] Chang, Y. B., and Moretti, P. M., 2002, "Flow Induced Vibration of Free Edge on Thin Film," Journal of Fluids and Structures, 16(7) pp. 989-1008.

[124] Morris-Thomas, M., and Steen, S., 2009, "Experiments on the Stability and Drag of a Flexible Sheet Under in-Plane Tension in Uniform Flow," Journal of Fluids and Structures, 25(5) pp. 815-830.

[125] Chen, C. J., 1992, "Electromechanical Deflections of Piezoelectric Tubes with Quartered Electrodes," Applied Physics Letters, 60(1) pp. 132-4.

[126] Smart Material, 2012, "Macro Fiber Composite - MFC," 2012.

[127] Wikipedia, 2013, "Hydraulic Diameter," 2013.

[128] Richter, D., Shaqfeh, E. S. G., and Iaccarino, G., 2011, "Floquet Stability Analysis of Viscoelastic Flow Over a Cylinder," Journal of Non-Newtonian Fluid Mechanics, 166(11) pp. 554-65.

[129] Guzeyev, A. S., and Dianov, D. I., 1991, "Separation Zones in Flow Over a Cylinder Base," Fluid Mechanics - Soviet Research, 20(5) pp. 40-3.

[130] Bansal, R. K., Sachdeva, R. C., and Seshadari, V., 1981, "Application of Finite Element Method to Potential Flow Over a Cylinder," Journal of the Institution of Engineers (India) Mechanical Engineering Division, 61pp. 175-80.

[131] Wickenheiser, A. M., and Garcia, E., 2010, "Power Optimization of Vibration Energy Harvesters Utilizing Passive and Active Circuits," Journal of Intelligent Material Systems and Structures, 21(13) pp. 1343-61.

[132] Yu-Yin Chen, Vasic, D., Costa, F., 2010, "Self-powered piezoelectric energy harvesting device using velocity control synchronized switching technique," IECON 2010 - 36th Annual Conference on IEEE Industrial Electronics Society, pp. 1785-1790.

[133] Liu, Y., Tian, G., Wang, Y., 2009, "Active Piezoelectric Energy Harvesting: General Principle and Experimental Demonstration," Journal of Intelligent Material Systems and Structures, 20(5) pp. 575-585.

[134] Lallart, M., Anton, S. R., and Inman, D. J., 2010, "Frequency Self-Tuning Scheme for Broadband Vibration Energy Harvesting," Journal of Intelligent Material Systems and Structures, 21(9) pp. 897-906.